Unveiling Nickel Chemistry in Stabilizing High-Voltage Cobalt-Rich Cathodes for Lithium-Ion Batteries

Moonsu Yoon, Yanhao Dong, Youngbin Yoo, Seungjun Myeong, Jaeseong Hwang, Junhyeok Kim, Seong-Hyeon Choi, Jaekyung Sung, Seok Ju Kang, Ju Li,* and Jaephil Cho*

A practical solution is presented to increase the stability of 4.45 V LiCoO₂ via high-temperature Ni doping, without adding any extra synthesis step or cost. How a putative uniform bulk doping with highly soluble elements can profoundly modify the surface chemistry and structural stability is identified from systematic chemical and microstructural analyses. This modification has an electronic origin, where surface-oxygen-loss induced Co reduction that favors the tetrahedral site and causes damaging spinel phase formation is replaced by Ni reduction that favors octahedral site and creates a better cation-mixed structure. The findings of this study point to previously unspecified surface effects on the electrochemical performance of battery electrode materials hidden behind an extensively practiced bulk doping strategy. The new understanding of complex surface chemistry is expected to help develop higher-energy-density cathode materials for rechargeable batteries.

1. Introduction

Lithium-ion batteries (LIBs) underly the energy infrastructure of our society.[1–4] Significant improvement in volumetric energy density is still in great demand today. For LIB cathodes, even though much progress has been made in Ni-rich layered cathode including the family of $LiNi_{1−x−y}Co_xMn_yO_2$ (NCM) and $LiNi_{1−x−y}Co_xAl_yO_2$ (NCA) chemistries (including single crystal NCM/NCA with ≈3.6 g cc⁻¹ electrode density), conventional $LiCoO_2$ (LCO) still holds the record for practical volumetric energy density (2600 Wh L⁻¹ when charged to 4.40 V versus Li/Li⁺; higher charge voltage is required to compete with single crystal NCM/NCA) due to its high compressed electrode

density (4.0–4.2 g cc⁻¹).[5–7] As a result, in applications where volume is the most precious and price is less of a problem (e.g., in smartphones), LCO would still hold a large portion of the market in the near future. Elevating the upper cutoff voltage in charging is the most straightforward method to further increase the energy density of LCO, but it unfortunately leads to poor cyclability if charged to >4.40 V versus Li/Li⁺ ($x \geq 0.6$ in the form of $Li_{1−x}CoO_2$).[8–13] Extensive researches in the past decades seek to address this critical issue. It is known that oxygen redox ($O^{2−} \leftrightarrow O^{1−}$) starts to contribute capacity at these higher voltages, since the O 2p orbitals hybridizes with the Co 3d orbitals in the $Co^{3+/4+}:t_{2g}$ & O 2p resonant band at lower electronic energies.[14] The peroxide ion $O^{1−}$ has higher ionic mobility than the oxide ion $O^{2−}$, and $O^{1−}$ near the surface are especially prone to leaving the LCO particle, which can happen even when there is no external current (i.e., the battery is supposed to be holding its charge). This disrupts the cathode–electrolyte interface, and the effluent oxygen will react with liquid electrolyte and burn up this scarce resource (only few gram (electrolyte)/Ah used in practical full cells), leaving voids and reduced transition metals (TM) behind. What then happen afterward inside LCO are not very clear, but there are theories and practices about mitigating the ill effects, by either i) suppressing irreversible phase transformations in the bulk LCO by bulk doping (e.g., Mg, Cr, Ti, Mn, and Al; Al/La codoping)[15–21] or ii) suppressing surface instabilities, including formation of spinel-phase and cathode–electrolyte interphase (CEI) by engineering LCO surface via various coating process (e.g., sol–gel process, chemical polymerization or deposition techniques).[7,22–25] While in practice both approaches improve the performance of LCO, the "bulk-phase" versus "surface-phase" dichotomy of this discussion seems a bit self-contradictory, since if mechanism (i) dominates, method (ii) should not work; and *vice versa*, if mechanism (ii) dominates, method (i) should not work. This is the scientific question we seek to address: what is the degradation mechanism of LCO and why both bulk doping and surface coating strategies help? Henceforth, through a sequence of carefully controlled experiments, we found how a putative uniform bulk doping could significantly affect the surface chemistry by surface segregation of Ni, and to show the "surface-phase" instability theory is correct. Surface segregation by bulk doping small amount of Ni is sufficient to reduce the degree of O anion redox near the surface, because

M. Yoon, Y. Yoo, Dr. S. Myeong,[+] J. Hwang, Dr. J. Kim, Dr. S.-H. Choi, J. Sung, Prof. S. J. Kang, Prof. J. Cho
Department of Energy Engineering
School of Energy and Chemical Engineering
Ulsan National Institute of Science and Technology (UNIST)
50 UNIST-gil, Ulsan 44919, Republic of Korea
E-mail: jpcho@unist.ac.kr
Dr. Y. Dong, Prof. J. Li
Department of Nuclear Science and Engineering & Department of Materials Science and Engineering
Massachusetts Institute of Technology
Cambridge, MA 02139, USA
E-mail: liju@mit.edu
The ORCID identification number(s) for the author(s) of this article can be found under https://doi.org/10.1002/adfm.201907903.

[+]Present address: Department of Materials, University of Oxford, Parks Road, Oxford OX1 3PH, UK

DOI: 10.1002/adfm.201907903

**ADVANCED
SCIENCE NEWS**
www.advancedsciencenews.com

**ADVANCED
FUNCTIONAL
MATERIALS**
www.afm-journal.de

the higher fraction of Ni on surface contributes to capacity without coupling to O $2p$ orbitals, due to the higher electronic energies of $Ni^{3+/4+}$:e_g compared to $Co^{3+/4+}$: t_{2g} & O $2p$ resonant band. The surface-enriched Ni also guides the O-loss induced instability toward a more stable surface cation-mixed phase outcome, rather than an unstable surface spinel-phase outcome that exacerbates the O-loss in a chain-reaction fashion.

In terms of practical applications, since LCO has already enjoyed great success in commercialization, we emphasize that any acclaimed improvements should be verified under industry-level conditions and the method should be cost-effective. These requirements shall be strictly followed in the present study. In this article, we show bulk-phase $LiCo_{0.95}Ni_{0.05}O_2$ (LCNO) has superior stability at high charge voltage of 4.45 V at practical conditions (loading density ≈15 mg cm^{-2}, electrode density ≈4.0 g cm^{-3} and areal capacity 2.5 mAh cm^{-2} with both coin-type half-cell and pouch-type full-cell testing). Previously, the effect of bulk Ni doping (and other elements such as Mg, Zr, and La) was interpreted as a "pillar effect": Ni^{2+} sharing similar charge and ionic radius as Li^+ would substitute at Octa-3a site in the Li-slab, thus preventing slab sliding at highly delithiated state.[26,27] While we do witness improved cyclability and suppressed bulk phase transitions upon bulk Ni doping, the previous interpretation should not be taken without challenge. While Ni doping only slightly changes the bulk chemistry, more pronounced surface effects, such as suppressed CEI formation and phase transformation in the close-to-surface region, were totally overlooked in the past.

2. Results and Discussion

Single crystalline LCNO (D_{50} of ≈10 μm) with the composition of "$LiCo_{0.95}Ni_{0.05}O_2$" and undoped LCO were prepared by conventional solid-state synthesis (see their microstructures in Figure S1, particle sizes and specific surface areas in Table S1, and chemical compositions and distributions were confirmed by transmission electron microscopy coupled with an energy dispersive X-ray spectrometer in Figure S2 and inductively coupled plasma-optical emission spectrometry in Table S2, respectively, Supporting Information). To obtain crystallographic parameters and atomic occupancies, Rietveld refinement was performed, which shows 0.9% Ni out of the total number of TM is located at Li-layer sites (LiL) in LCNO (Figure S3 and detailed fitting parameters in Table S3, Supporting Information). This antisite defect Ni_{LiL} (so-called "cation mixing") forms because of similar charge and ionic radius of Ni^{2+} and Li^+, whose mixing level becomes larger at higher temperatures and in a less-oxidizing atmosphere where Ni^{2+} is thermodynamically favored over Ni^{3+}.[28,29] Apparently, this high level of cation mixing in LCNO (relative to the amount of Ni we put in) originates from the synthesis condition (i.e., high temperature of 970 °C in air).

The electrochemical properties of LCNO were first evaluated by half cells at 3.0–4.45 V versus Li/Li$^+$, and the cyclic performance at a current rate of 1.0 C (185 mA g^{-1}) are displayed in **Figure 1**a,b (the formation cycle for each cell was conducted at 0.1 C, Figure S4, Supporting Information). Interestingly, LCNO have demonstrated the better cycling stability with a high capacity retention of ≈93% (165 mAh g^{-1}) during 100 cycles,

compared to ≈73% capacity retention (131mAh g^{-1}) of LCO. LCNO also has a higher average Coulombic efficiency (CE) of 99.69% for the first 100 cycles, compared to that of 98.72% for LCO, when charged to 4.45 V versus Li/Li$^+$. Furthermore, the charge/discharge curves of LCNO have rarely changed, while that of LCO exhibits a dramatic change upon cycling (Figure 1b). Meanwhile, as shown in Figure 1c, LCNO also demonstrates better rate performance than LCO, with less capacity decrease from 0.2C (0.51 mA cm^{-2}) to 5C (12.80 mA cm^{-2}). Specifically, LCNO demonstrated an impressive discharge capacity of 150.2 mAh g^{-1} at 5 C with less overpotentials, while LCO has only 116.2 mAh g^{-1} at 5 C (Figure S5, Supporting Information).

Next, to evaluate the long-term cycling performance of LCNO in a more practical way, pouch-type full-cell testing was performed in the *full-cell* voltage range of 3.0–4.35 V (Figure 1d). Spherical graphite (Gr) is used as anode in full cells, exhibiting stable cycling properties with an average voltage of 0.15 V in the Gr/Li half cell (Figure S6, more details on electrode specifications, testing conditions, and energy density calculation method are given in Table S4 and Note S1, Supporting Information). LCNO/Gr full cell shows better cycling stability and higher CE that than LCO/Gr at both 25 °C (Figure 1d and Figure S7, Supporting Information) and 45 °C (Figure S8, Supporting Information), which agree with the half-cell results. Specifically, at 25 °C, LCNO/Gr full cell demonstrates superior energy density of 601 Wh L^{-1} (92% retention) after 500 cycles, compared with 514 Wh L^{-1} (79% retention) for LCO/Gr. Moreover, the working voltage (average discharge voltage) of LCNO/Gr full cell stably maintains at around 3.82 V over 500 cycles, while that of LCO/Gr gradually drops to 3.78 V. Therefore, LCNO demonstrates superior electrochemical performance in both half and full cells over LCO at the high voltage.

Now that the experimental advantage of slight Ni bulk doping is obvious, we seek to understand the underlying mechanism. As mentioned above, previous studies attributed (A) improved cyclability of Ni doped LCO to a "pillar effect" based on the observation of concurrent (B) suppressed phase transitions at high voltages (i.e., the case showing both A and B). The latter was also observed in the present work, as illustrated in the differential capacity versus voltage (dQ/dV) plot of the first charge/discharge curve of in **Figure 2**a. There are two peaks at 4.1 V and 4.2 V due to the phase transition from the hexagonal (O3) to monoclinic phase[30] and the other peak at 4.4 V represents the O3–(H1–3) phase transition in LCO,[31,32] while they become much weaker in LCNO. However, to explain (A) improved cyclability by (B) suppressed phase transitions in the bulk needs more thoughtful considerations. First of all, the transformed phases such as O2-type LCO have high electrochemical capacity as well as high Li$^+$ and electronic conductivities, so it is not straightforward why such bulk phase transitions necessarily lead to degradation.[33] Second, surface coating has been frequently practiced to improve high-voltage cyclability of LCO. While its benefit is undeniable, it does not suppress any bulk phase transitions at all (i.e., the case showing A but not B).[24,34,35] Third, some studies of bulk doping show suppressed phase transitions yet there were no improvements in high-voltage cyclability (i.e., the case showing B but not A).[36] So (B) is neither a necessary nor sufficient condition
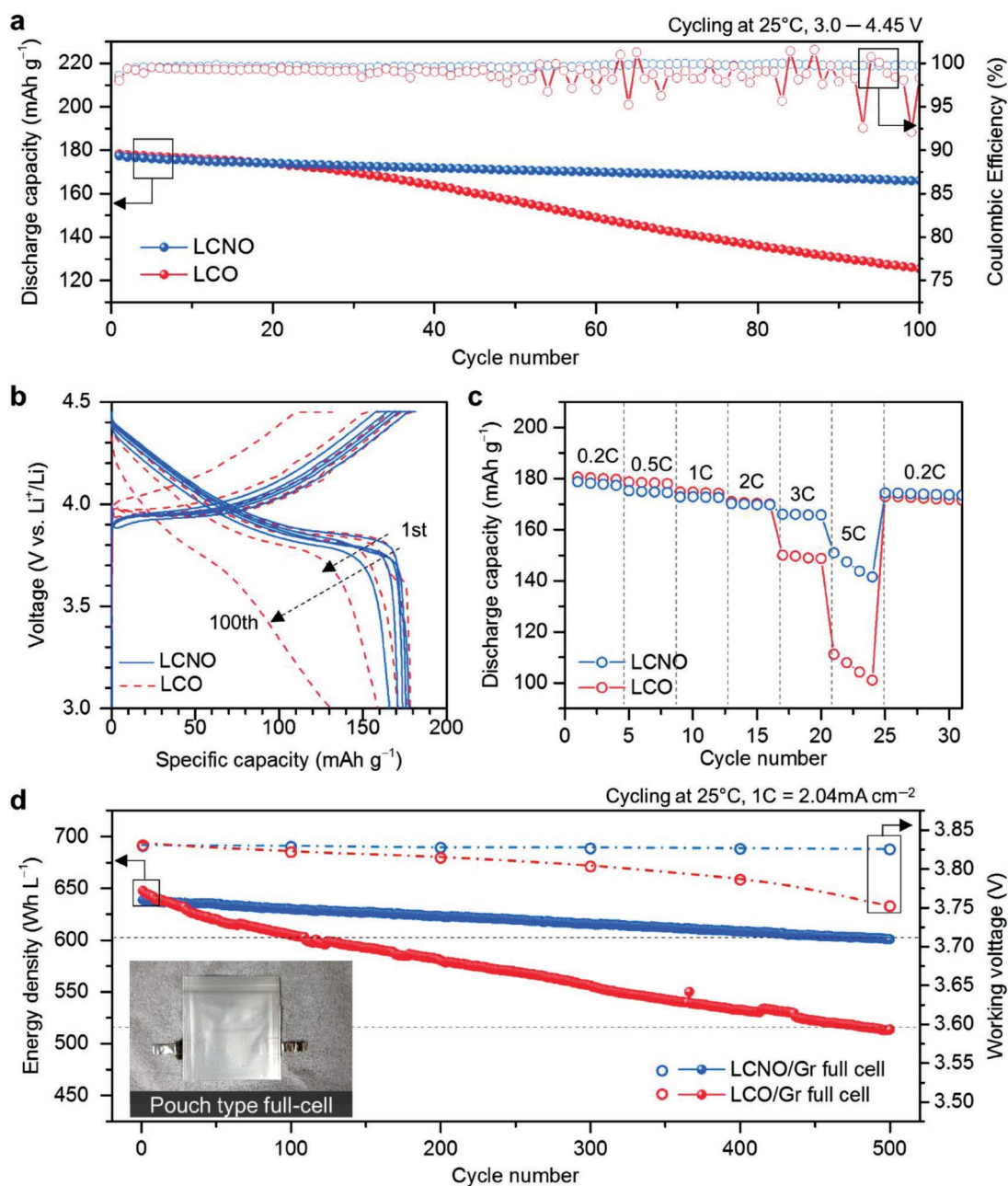
Figure 1. Electrochemical performance of LCO and LCNO cells. a) Galvanostatic charge–discharge test of the LCNO and LCO electrodes at 25 °C, where the operating voltage range of 3.0–4.45 V (vs Li/Li⁺) with charge and discharge of 1C. b) Voltage profiles corresponding to 1st, 5th, 25th, 50th, and 100th cycles. c) Rate performance from 0.2 C to 5 C measured at 25 °C. d) Cycling performance of LCNO/Gr and LCO/Gr full cells for 500 cycles.

of (A). Furthermore, according to ex situ X-ray diffraction (XRD) of cycled LCO and LCNO in Figure 2b and Figure S9 (Supporting Information), the irreversible bulk phase transition in LCO (from O3 to H1–3, evidenced by shifting of (003) peak at $2\theta = 18.9°$ and fading of (006) peak at 38.4°) does not occur during the first 100 cycles, yet the capacity decay is continuous from the very beginning and accelerated degradation starts from early 20 cycles. Therefore, although Ni doping does suppress bulk phase transitions during charge–discharge process, it cannot be the main reason for the improved cyclability.

Meanwhile, we noted marginal effect of 5% Ni on the bulk redox of LCO. The dQ/dV curve of LCNO has similar shape with LCO (Figure 2a), except for the early stage of charge below 3.9 V due to $Ni^{+3/+4}$ redox.[37] This conclusion is further supported by first-principles calculations, which identify similar electronic density of states (DOS) for LCO (Figure S10 for stoichiometric $LiCoO_2$ and to be shown in Figure 5b for delithiated $Li_{0.333}CoO_2$, Supporting Information) and LCNO (Figure S11 for stoichiometric $LiNi_{0.074}Co_{0.926}O_2$ and Figure S12 for delithiated $Li_{0.333}Ni_{0.074}Co_{0.926}O_2$, Supporting Information). These

**ADVANCED
SCIENCE NEWS**

www.advancedsciencenews.com

**ADVANCED
FUNCTIONAL
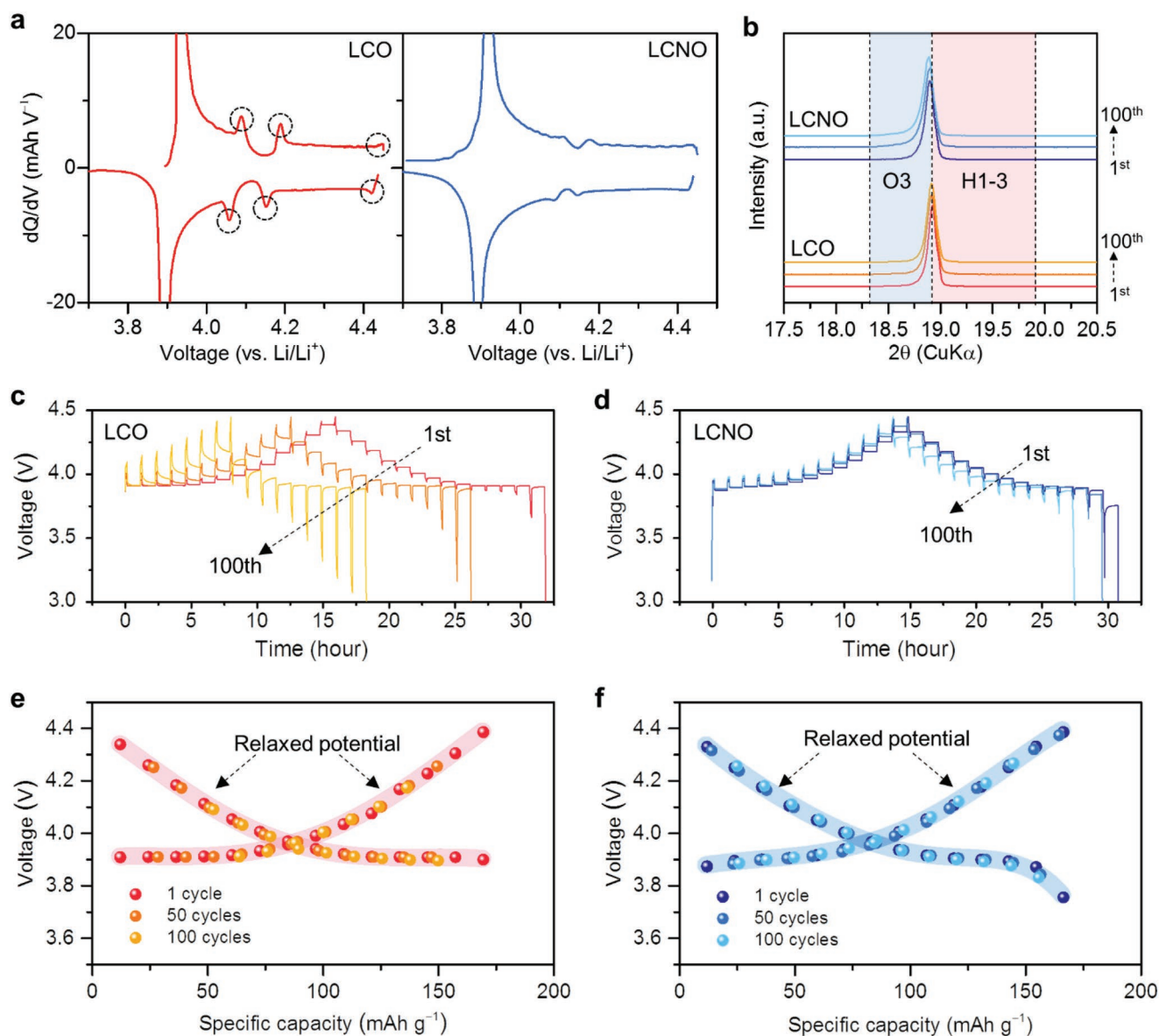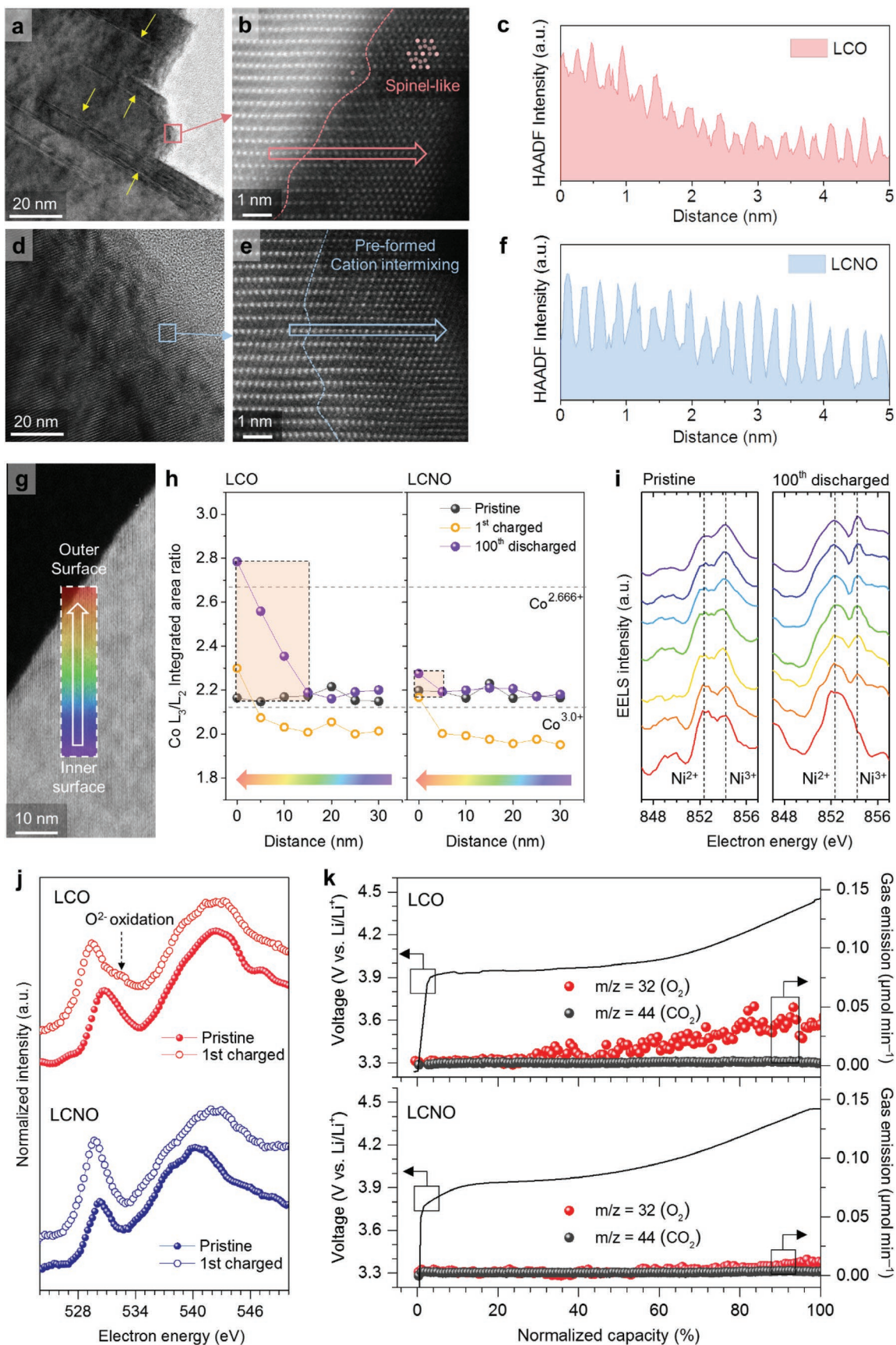MATERIALS**

www.afm-journal.de

Figure 2. Electrochemical analyses of LCO and LCNO electrodes. a) Comparison of dQ/dV plot for cell with LCO and LCNO electrode in the voltage range of 3.0–4.45 V (vs Li/Li$^+$). b) Magnified ex situ XRD patterns between $2\theta = 17.5°$ and $20.5°$ for 1st, 50th and 100th cycled LCO and LCNO. c,d) Voltage–time profiles of GITT for LCNO and LCO measured at 1st, 50th and 100th cycle, and e,f) their voltage profiles under OCV conditions.

observations leave an intriguing question: If suppressing bulk phase transitions does not help much and bulk redox thermochemistry is barely changed, how could bulk Ni doping work?

Before answering the question, we first investigate whether the degradation has a thermodynamic or kinetic origin, via galvanostatic intermittent titration technique (GITT) characterizations for LCO and LCNO conducted at 1st, 50th and 100th cycles (Figure 2c,d). For pristine LCO and LCNO, the overpotentials are small at all states of charge (except for the end of discharge), indicating good transport kinetics of Li$^+$ and electrons in the electrode composites (of active materials, carbon, binder and electrolyte-soaked porosity). Yet, for LCO, 4.45V-cycling induced a dramatic overpotential growth, while the increment is much smaller in LCNO. Interestingly, if we exclude such voltage

losses (i.e., overpotential) due to either Li$^+$ or electron transport (in either electrode composites or LCO/LCNO particles) and plot the relaxed potentials after each titration step as a function of discharge capacity (mimicking charge/discharge curve under open circuit condition), the data before and after cycling coincide into one curve nicely for both LCO and LCNO (Figure 2e,f; more detailed provided in Note S2, Supporting Information). It clearly demonstrates that capacity decay in LCO and LCNO is mostly from growth of internal impedance from sluggish kinetics rather than changes in redox chemistry and thermodynamics.[24,38] The conclusion is further supported by electrochemical impedance spectroscopy (EIS) measurements, which show over-growth of charge transfer resistance (calculated from the semicircle radius of the middle-to-low frequencies) in the

**ADVANCED
SCIENCE NEWS**
www.advancedsciencenews.com

**ADVANCED
FUNCTIONAL
MATERIALS**
www.afm-journal.de

Nyquist plots of cycled LCO, while the change is much smaller in LCNO (Figure S13, Supporting Information). We also noted that the XRD results indicate minimum structural change of both LCO and LCNO during the first 100 cycles (Figure S9, Supporting Information), thus the accelerated capacity decay in LCO cells cannot be dominantly influenced by irreversible structural changes in the bulk materials either. Without any evident changes in either redox chemistry or atomic structure and with clearly observed impedance growth, we conclude that the degradation of doped/undoped LCO is critically coupled with a kinetic rather than a thermodynamic origin.

We now provide a simple, consistent explanation of the above seemingly disparate observations: A putative uniform Ni doping also modifies the surface of LCO by surface segregation, which is critical to its electrochemical stability. This is supported by the following experimental findings. First, the surface of pristine LCO particles has a layered structure (space group R$\bar{3}$m, same with bulk phase) as shown by TEM in Figure S14 (Supporting Information). However, it reconstructs extensively after cycling, in the form of phase transition to Co$_3$O$_4$-like spinel structure (space group Fd$\bar{3}$m, 5–10 nm thick after 100 cycles; it is known to have sluggish Li$^+$ diffusivity)[39] and microcrack formation as shown in **Figure 3**a,b. Furthermore, the high-angle annular dark-field (HAADF) signal intensity significantly decreased at the surface, indicating a large amount of TM defects were generated after cycling (Figure 3c), or a rough surface. In contrast, the surface of LCNO has a cation-mixed layered structure with ≈3 nm thickness before (Figure S15, Supporting Information) and after cycling (Figure 3d,e) and no microcracks were observed. Little variation of HAADF signal (Figure 3f) from the surface to the bulk indicates much less TM defects/surface roughness compared to LCO (Ni segregation at the surface of LCNO is supported by spatially resolved electron energy-loss spectroscopy (EELS) data of pristine and cycled LCNO in Figure S16, Supporting information). Therefore, Ni doping modifies the surface structure of LCO, which does not evolve as significant as undoped LCO upon cycling.
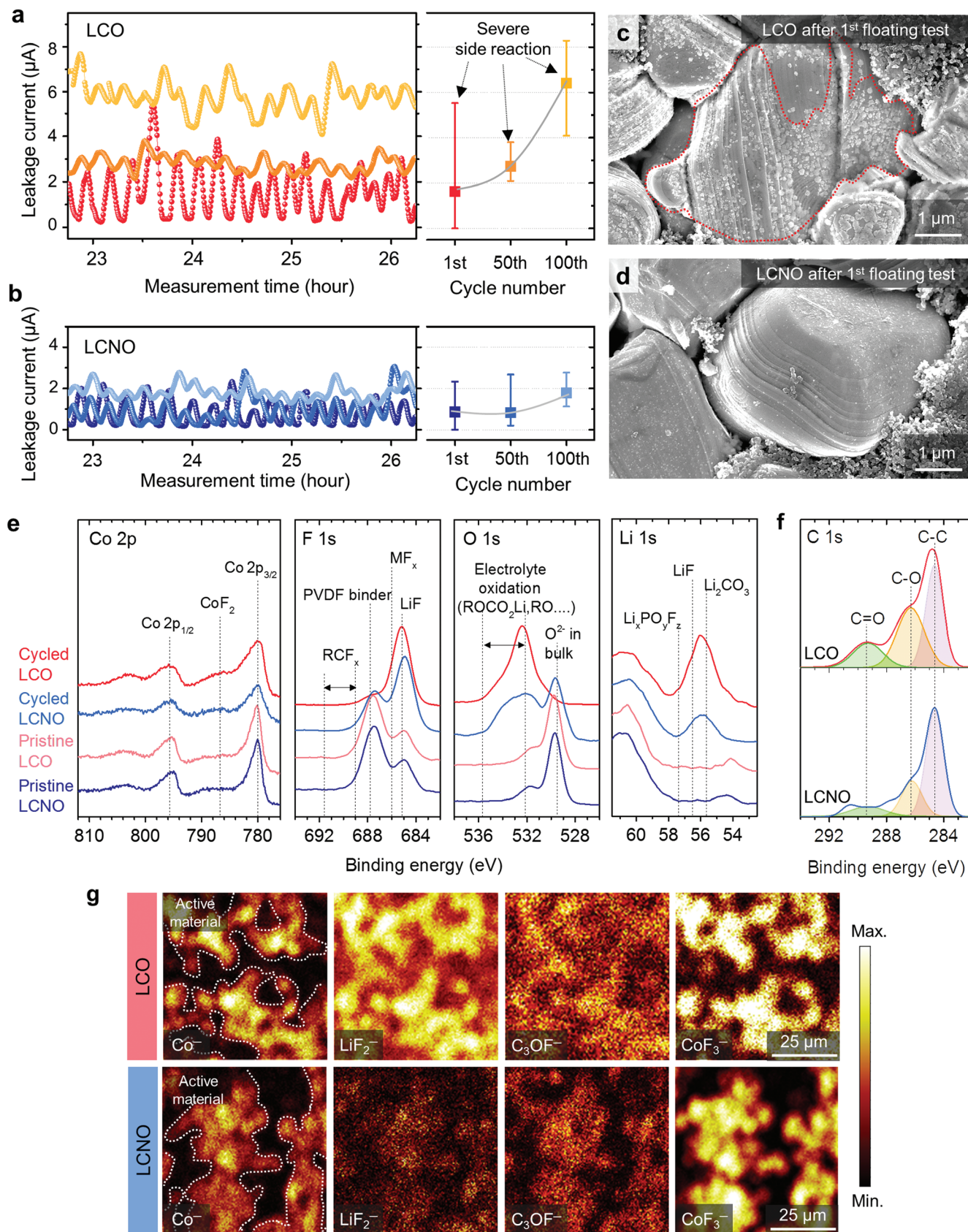
Second, spatially resolved EELS reveals less reduction of Co at the surface of LCNO than LCO after 1st charge and after 100th discharge (Figure 3g–i). (L$_3$/L$_2$ intensity ratios of standard references LiCoO$_2$, Co$_3$O$_4$, and CoO were used to identify Co^{3+}, Co$^{2.666+}$, and Co^{2+}, respectively; for more details, see Figures S17 and S18 and Note S3, Supporting Information). In pristine LCO, we found constant valence/local chemical environment of Co^{3+} at 0–35 nm from the surface (Figure 3h). However, when LCO is first charged to 4.45 V versus Li/Li$^+$, Co at the surface becomes lower in valence, which is in contrast with oxidation of Co in the bulk (to compensate charge of del-ithiation). The surface reduction implies massive side reaction between charged LCO and electrolytes, leading to significaition surface reconstruction.[40–42] This process continues upon cycling, resulting in greatly reduced Co close to Co$^{2.666+}$ after 100 cycles, which is consistent with the observed Co$_3$O$_4$-like structure in Figure 3b. In contrast, Co is less reduced in LCNO than in LCO, implying that less side reactions and surface reconstruction (right panel of Figure 3h). One thing to note is that even though some Ni^{3+} are reduced to +2 at the surface of LCNO (decrease in shoulder peak of Ni^{3+} species, at ≈854 eV, in Figure 3i),[43] its surface remains similarly cation-mixed structure before and after cycling. Increased anti-site defect of Ni$_{LiL}$ in cycle LCNO also indicates reduced Ni^{2+} is stably incorporated with preformed cation-mixied structure (Figure S19 and Table S5, Supporting Information).

Considering the strong correlations (but with time delays) between oxygen anion-redox, oxygen mobility and loss, surface instability and cation transformations at high voltage, the investigation of surface oxygen states would shed light on the mechanism of improvement by Ni doping. In O K-edge, the pre-edge corresponds to transition from O core 1s to the unoccupied hybridized band state of O 2p and TM 3d orbitals, indicating the hole states in TM–O bonding.[44] Interestingly, when the prepared cathodes were first charged to 4.45 V, we observed a small shoulder (at 528–533 eV) for LCO outer surface but not for LCNO (Figure 3j and Figure S20, Supporting Information), which indicates an suppressed oxidation of O^{2-} in LCNO surface during charge.[13,45] Since the oxidation of O^{2-} (forming mobile peroxo O^{1-}) results in serious side reactions due to oxygen loss and high chemical reactivity toward electrolyte, we believe less O^{1-} generation *on surface* must be beneficial.[41,46,47] Ni segregation helps in this regard, because the higher fraction of Ni on surface contributes to capacity without coupling to O 2p orbitals, due to the higher electronic energies of Ni$^{3+/4+}$:e$_g$ compared to Co$^{3+/4+}$:t$_{2g}$ & O 2p resonant band.[14] Consistently, there is less gas evolution for LCNO than LCO during first charge, as supported by in situ differential electrochemical mass spectrometry (DEMS) data in Figure 3k. Therefore, Ni-modified surface structure effectively suppresses oxidation of O^{2-} species, thereby experiences less TM reduction and oxygen loss upon charge and cycling.

Third, we conducted floating test (an established method to evaluate the voltage window of electrolytes)[48,49] to investigate the surface reactivity of LCO and LCNO. Half cells after 1st, 50th, and 100th cycles (at 0.2C) were charged to 4.45 V versus Li/Li$^+$, maintained under constant voltage for 27 hours under 60 °C while recording the leakage current. During the long-time high-temperature holding, the leakage current must come from side reactions between charged LCO/LCNO and organic electrolyte. As shown in **Figure 4**a,b, the leakage current density

Figure 3. Stabilized LCNO surface showing less reconstruction, TM reduction, and oxygen loss. a) Surface microstructure of the LCO with microcracks after 100 cycles at 25 °C half-cell. b) Magnified HAADF-STEM images corresponding to selected region of (a), showing Co$_3$O$_4$-like spinel. c) Declining HAADF-signal profile of the cycled LCO for selected region in (b). d) Surface microstructure of 100th cycled LCNO showing no cracks. e) Magnified HAADF-STEM image corresponding selected region of (d), showing inner and outer surfaces were stably maintained as layered and cation-mixing structures, respectively. f) Well-maintained HAADF-signal profile of the cycled LCNO for selected region in (e). g) Schematic EELS scanning pathway (0–35 nm from surface). h) Co L$_3$/L$_2$ ratio analysis based on the collected Co L-edge at each state. The black dotted lines indicate the oxidation state of Co as 2.66$^+$ and 3.00$^+$ (from top to bottom), respectively. Co L$_3$/L$_2$ ratio for pristine, 1st charged and 100th discharged LCO and LCNO, showing less Co reduction for LCNO. i) Ni L$_3$-edge spectra for the pristine and cycled LCNO showing more Ni reduction at the surface and after cycling. j) The comparison between pre-edge of O K-edge EELS spectra corresponding to the outermost surface region for each pristine and 1st charged LCO and LCNO, suggesting less oxidization of O^{2-} in LCNO surface. k) In situ DEMS analyses in coin-type half cell with LCO and LCNO during first charge.

ADVANCED
SCIENCE NEWS
www.advancedsciencenews.com

ADVANCED
FUNCTIONAL
MATERIALS
www.afm-journal.de

**ADVANCED
SCIENCE NEWS**

www.advancedsciencenews.com

**ADVANCED
FUNCTIONAL
MATERIALS**

www.afm-journal.de

of LCO is larger than that of LCNO at initial cycle and their difference magnifies upon cycling. Consistent results were also obtained by performing the same floating tests at higher charge voltage of 4.5–4.7 V versus Li/Li$^+$ (Figure S21, Supporting Information), where LCNO always has much smaller leakage current density. Considering the similar particle size and specific surface area (see Brunauer–Emmett–Teller, BET data in Table S1 of LCO and LCNO, Supporting Information), the above results prove Ni-modified surface structure indeed reduces chemical reactivity of LCO toward the organic electrolyte. Since practical full-cells use very little electrolyte (few gram/Ah), this bodes well for the long-term shelf life and cycle life of the LCNO battery.

Fourth, the lowered chemical reactivity results in less CEI formation of LCNO than LCO. This is evidenced by X-ray photoelectron spectroscopy (XPS) and time-of-flight secondary ion mass spectrometry (TOF-SIMS) data collected on LCO and LCNO before and after 100 cycles in half-cell testing. As shown by XPS in Figure 4e, the signal of lattice O^{2-} has a strong peak at ≈530 eV in pristine LCO and LCNO. However, it decays to zero with an emerging peak at 532–533 eV (from O 1s orbital of oxidation products of electrolytes) for cycled LCO, while its intensity is better maintained in cycled LCNO. Similarly, there is weaker intensity for the peak at ≈56 eV (from Li 1s orbital of Li-containing compound, such as resistive LiF and Li$_2$CO$_3$) in cycled LCNO than in cycled LCO. In particular, one thing to note is that in C 1s region of cycled LCO, a dramatic increase of the C 1s peak characteristics of C–O (C 1s, 286 eV) and C=O (C 1s, 289 eV) bonds in ≈2:1 ratio upon cycling would be expected for mass generation of PEC, a result of ethylene carbonate (EC) decomposition (Figure 4f).[50] These features coherently suggest that on LCNO surface, side reactions including not only EC ring-opening but also PF$_6^-$, counterion of salt, to form PF$_5$ and HF,[51,52] are significantly suppressed. As illustrated in Figure 4g, consistent trend is also found in TOF-SIMS mapping, showing less accumulation of CEIs species (e.g., ^{7}LiF$_2^-$, C$_3$OF$^-$, CoF$_3^-$, CH$_3$O$^-$, C$_2$HO$^-$, and C$_2$F$^-$ from electrolyte decomposition)[53,54] on the surface of LCNO than that of LCO (for more details, see Figures S22 and S23 and Table S6, Supporting Information). Furthermore, as the floating test at high temperature and high voltage can be viewed as an accelerated degradation experiment, the over-grown CEI enriched with C and F signals on the surface of LCO after 1st charge to 4.45 V (vs Li/Li$^+$) and 27 h's hold at 60 °C can be vividly seen under scanning electron microscope (SEM) in Figure 4c and Figure S24 (Supporting Information), while that of LCNO can hardly be detected visually in Figure 4d. Therefore, Ni-modified surface structure indeed reduces the formation and growth of CEI at high voltages and during prolonged cycling.

Lastly, we rationalized the improved surface stability of LCNO via first-principles calculations, by comparing the calculated electronic density of states (DOS) of Li$_{0.333}$CoO$_2$ in **Figure 5**a

(corresponding to delithiated LCO) and Li$_{0.111}$Ni$_{0.296}$Co$_{0.926}$O$_2$ in Figure 5d, that is a delithiated cation-mixed structure similar to the surface of LCNO, which has the same state of charge as Li$_{0.33}$CoO$_2$; here, 0.222 Ni per formula is at Li-slab and the remaining 0.074 is at TM-slab, so it can be written as (Li$_{0.111}$Ni$_{0.222}$)(Ni$_{0.074}$Co$_{0.926}$)O$_2$.

Unlike Li$_{0.333}$CoO$_2$ which has overlapping valence-band and conduction-band states similar to a semi-metal, Li$_{0.111}$Ni$_{0.296}$Co$_{0.926}$O$_2$ has a small band gap of 0.3 eV, which reduces DOS at the Fermi level (Figure 5b,e). From electronic perspective, this feature lowers the energy of highest occupied states and limits electron transfer from carbonate-based electrolyte dissociation, thus consequently stabilizing the cathode–electrolyte interface.[42,46,55] A quantitative comparison between Li$_{0.333}$CoO$_2$ and Li$_{0.111}$Ni$_{0.296}$Co$_{0.926}$O$_2$ is shown in Figure 5c,f, where the total DOS (in black) and projected DOS of O 2p orbitals (in red) at −0.8 to 0 eV versus Fermi level are plotted. Obviously, Li$_{0.111}$Ni$_{0.296}$Co$_{0.926}$O$_2$ (Figure 5c) has much less DOS than Li$_{0.333}$CoO$_2$ (Figure 5f), which supports the experimental findings of its reduced surface reactivity.

With the above information, a unified picture governing the stability and degradation kinetics of LCO/LCNO can be provided, which is schematically plotted in **Figure 6**. For undoped LCO, it suffers from severe surface oxygen loss and Co reduction from +3 to +2 during 1st charge. It triggers surface phase transition and cation densification to a Co$_3$O$_4$-like spinel structure during discharge (Co^{2+} migration to tetrahedral site, which stabilizes the electronic structure of Co^{2+}: $e_g^4 t_{2g}^3$; Co$_3$O$_4$ is a well-known normal spinel structure, with tetrahedral Co^{2+} and octahedral Co^{3+}), whose compact structure and small interstitial sites impedes Li$^+$ intercalation/diffusion. When this transformed surface layer undergoes charging again, it cannot be delithiated yet Co^{2+} is still prone to oxidation, which forces Co$_3$O$_4$ to decompose, Co ion to dissolve (see data of dissolved Co in electrolyte of cycled LCNO/Gr pouch-type full cell at 45 °C in Table S7, Supporting Information), oxygen to lose, much side reactions to happen, and extensive CEI to form in a chain-reaction fashion. The growth of resistive CEI and Co$_3$O$_4$-like surface structure increase the internal impedance continuously, which makes the degradation of LCO an accumulative and self-accelerating process. In comparison, the situation is greatly improved for LCNO. Albeit of smaller extent, LCNO also loses some surface oxygen during the 1st charge. But it is accompanied by Ni reduction from +3 to +2, rather than Co. This leaves the surface structure a cation-mixed structure (Ni^{2+} migration to octahedral site, because Ni^{2+} has a large radius similar to Li$^+$ and octahedral crystal field stabilizes Ni^{2+}: $t_{2g}^6 e_g^2$), which has larger lattice parameter and allows Li$^+$ intercalation/diffusion. Furthermore, Ni-modified cation-mixed structure has lower-energy HOMO, which also reduces the side reactions. Both factors cut off the positive-feedback-loop of accelerated degradation,

---

Figure 4. Investigating surface reactivity of cathode to electrolyte and suppressed CEI formation at surface. Leakage current of 1st, 50th, 100th cycled a) LCO and b) LCNO in floating tests. SEM of c) LCO and d) LCNO after floating tests for electrodes after 1st cycle. e) XPS spectroscopic data of LCO and LCNO electrodes before/after cycling: Co 2p, F 1s, O 1s, and Li 1s. Spectra of the cycled and pristine electrode are displayed from the top to bottom. f) XPS spectroscopic data after cycling: C 1s. Note that the C 1s peaks characteristics of C–O (C 1s, 286 eV) and C=O (C 1s, 289 eV) bond in ≈2:1 ratio, an indicator of PEC evolution, are significantly observed in cycled LCO. g) Top view TOF-SIMS data for LCO and LCNO after cycling. The active material in cycled LCNO electrodes are less covered by CEI, mainly composed of organofluorines compound (C$_3$OF$^-$) and HF attack resultant species (^{7}LiF$_2^-$, CoF$_3^-$).

**ADVANCED
SCIENCE NEWS**
www.advancedsciencenews.com

**ADVANCED
FUNCTIONAL
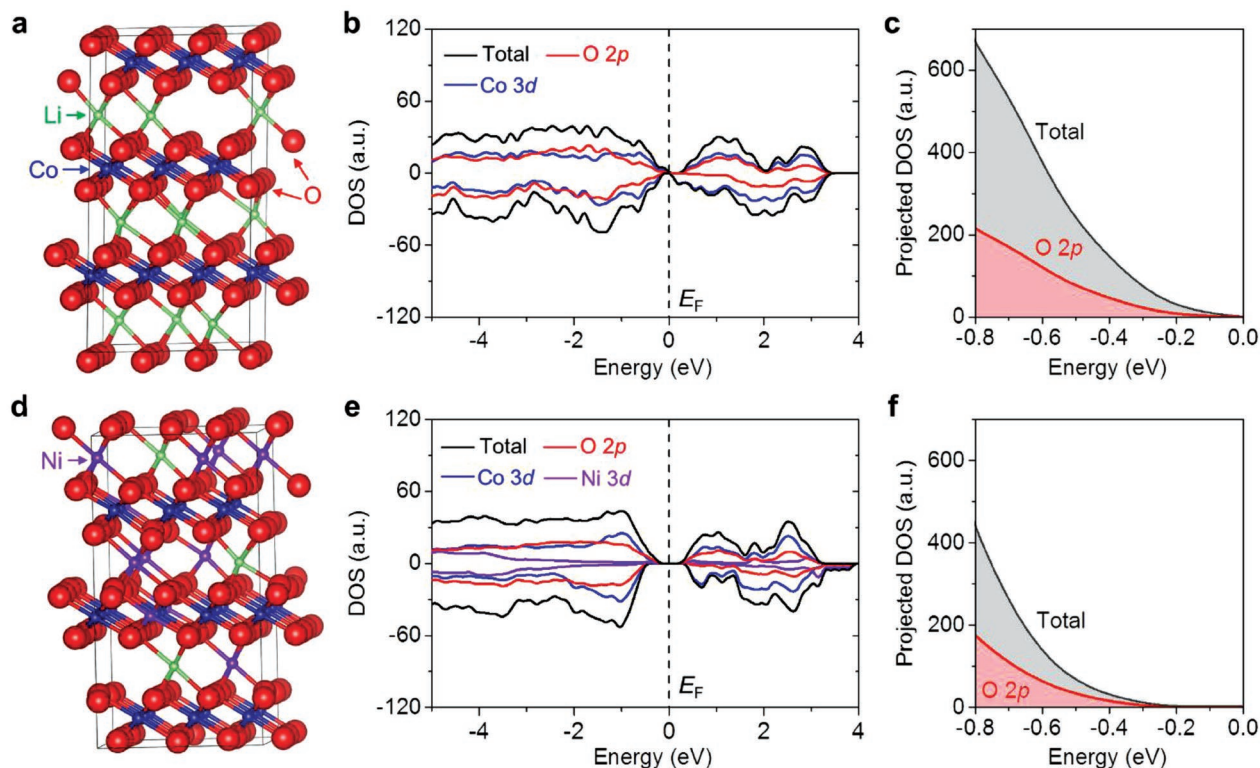MATERIALS**
www.afm-journal.de

Figure 5. First-principles calculations showing less DOS around Fermi level for LCNO. a) Atomic structure, b) DOS, and c) available states at −0.8 to 0 eV below Fermi level of $Li_{0.333}CoO_2$ simulating delithiated LCO. d) Atomic structure, e) DOS, and f) available states at −0.8 to 0 eV below Fermi level of $Li_{0.111}Ni_{0.296}Co_{0.926}O_2$ simulating delithiated cation-mixed surface phase of LCNO. Fermi level is set to be 0 eV.
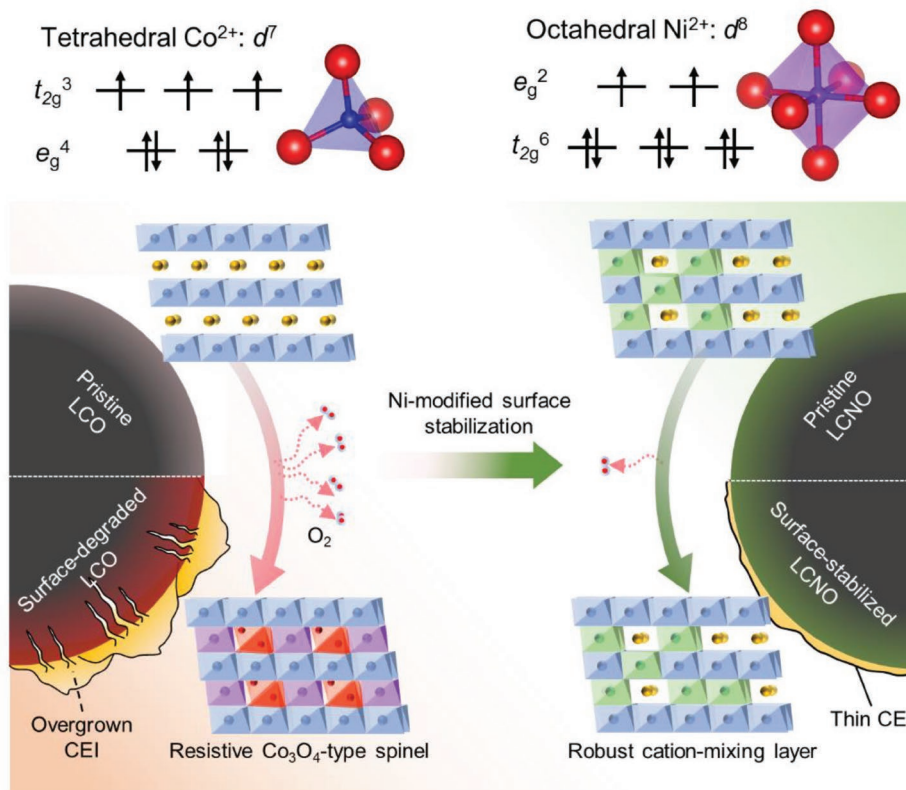
Figure 6. Schematic degradation mechanism of LCO and LCNO.

**ADVANCED
SCIENCE NEWS**

www.advancedsciencenews.com

**ADVANCED
FUNCTIONAL
MATERIALS**

www.afm-journal.de

which contributes the experimentally confirmed cycling stability of LCNO. Lastly, we emphasize the beneficial effect of Ni/Li interlayer mixing in stabilizing LCO surface shall not be confused with the situation in Ni-rich cathodes. The latter materials are known to suffer from a high level of bulk Ni/Li interlayer mixing even in the pristine samples synthesized in oxygen atmosphere and the mixing is more severe at the surface and after cycling. It finally leads to the formation of rock-salt NiO-like structure at the surface, which is harmful because of poor Li^+ and electron conductivities and causes cell failure. In comparison, in our LCNO samples, even though there is relatively more Ni/Li interlayer mixing at the surface than in the bulk, it is still minor and much less than the mixing level in Ni-rich cathodes. As a result, the surface of LCNO samples has a partially cation-mixed structure (not rock-salt NiO-like structure as is the case for Ni-rich cathodes) even after prolonged cycling, which is helpful and does not degrade the cell.

3. Conclusion

To summarize, we present a practical solution to increase the stability of 4.45 V $LiCoO_2$ via high-temperature Ni doping, without adding any extra synthesis steps or cost. This simple method can be combined with further surface modifications and such experiments are in progress to develop stable 4.6 V $LiCoO_2$. On the scientific side, we identified how a long putative uniform bulk doping with highly soluble elements can profoundly modify the surface structure and chemistry, which is critical to the electrochemical performance. This modification has an electronic origin, where surface-oxygen-loss induced Co reduction that favors tetrahedral site and causes damaging spinel phase formation is replaced by Ni reduction (a "sacrificial" cation, bearing the same spirit of sacrificial anodes in corrosion) that favors octahedral site and creates a better cation-mixed structure as more stable CEI substrate. Our findings point to many unknown surface effects on the electrochemical performance of battery electrode materials hidden behind extensively practiced bulk doping strategy.[56] The new understanding of complex surface chemistry is expected to help develop higher-energy-density cathode materials for battery applications.

Supporting Information

Supporting Information is available from the Wiley Online Library or from the author.

Acknowledgements

Conflict of Interest

The authors declare no conflict of interest.

Keywords

[1] D. Larcher, J. M. Tarascon, *Nat. Chem.* **2015**, *7*, 19.
[2] B. Dunn, H. Kamath, J.-M. Tarascon, *Science* **2011**, *334*, 928.
[3] M. M. Thackeray, C. Wolverton, E. D. Isaacs, *Energy Environ. Sci.* **2012**, *5*, 7854.
[4] J. B. Goodenough, Y. Kim, *Chem. Mater.* **2010**, *22*, 587.
[5] A. Manthiram, J. C. Knight, S.-T. Myung, S.-M. Oh, Y.-K. Sun, *Adv. Energy Mater.* **2016**, *6*, 1501010.
[6] J. Kim, H. Ma, H. Cha, H. Lee, J. Sung, M. Seo, P. Oh, M. Park, J. Cho, *Energy Environ. Sci.* **2018**, *11*, 1449.
[7] S. Kalluri, M. Yoon, M. Jo, S. Park, S. Myeong, J. Kim, S. X. Dou, Z. Guo, J. Cho, *Adv. Energy Mater.* **2017**, *7*, 1601507.
[8] T. Ohzuku, A. Ueda, *Solid State Ionics* **1994**, *69*, 201.
[9] J. Cho, Y. J. Kim, B. Park, *J. Electrochem. Soc.* **2001**, *148*, A1110.
[10] Z. Chen, J. R. Dahn, *Electrochim. Acta* **2004**, *49*, 1079.
[11] J. Kikkawa, S. Terada, A. Gunji, T. Nagai, K. Kurashima, K. Kimoto, *J. Phys. Chem. C* **2015**, *119*, 15823.
[12] J.-N. Zhang, Q. Li, Y. Wang, J. Zheng, X. Yu, H. Li, *Energy Storage Mater.* **2018**, *14*, 1.
[13] R. Hausbrand, G. Cherkashinin, H. Ehrenberg, M. Gröting, K. Albe, C. Hess, W. Jaegermann, *Mater. Sci. Eng., B* **2015**, *192*, 3.
[14] A. Manthiram, *ACS Cent. Sci.* **2017**, *3*, 1063.
[15] H.-J. Kim, Y. U. Jeong, J.-H. Lee, J.-J. Kim, *J. Power Sources* **2006**, *159*, 233.
[16] J. H. Cheng, C. J. Pan, C. Nithya, R. Thirunakaran, S. Gopukumar, C. H. Chen, J. F. Lee, J. M. Chen, A. Sivashanmugam, B. J. Hwang, *J. Power Sources* **2014**, *252*, 292.
[17] S. Madhavi, G. V. Subba Rao, B. V. R. Chowdari, S. F. Y. Li, *Electrochim. Acta* **2002**, *48*, 219.
[18] J. Yu, Z. Han, X. Hu, H. Zhan, Y. Zhou, X. Liu, *J. Power Sources* **2014**, *262*, 136.
[19] A. Liu, J. Li, R. Shunmugasundaram, J. R. Dahn, *J. Electrochem. Soc.* **2017**, *164*, A1655.
[20] F. Zhou, W. Luo, X. Zhao, J. R. Dahn, *J. Electrochem. Soc.* **2009**, *156*, A917.
[21] Q. Liu, X. Su, D. Lei, Y. Qin, J. Wen, F. Guo, Y. A. Wu, Y. Rong, R. Kou, X. Xiao, F. Aguesse, J. Bareño, J. Ren, W. Lu, Y. Li, *Nat. Energy* **2018**, *3*, 936.
[22] Y.-C. Lu, A. N. Mansour, N. Yabuuchi, Y. Shao-Horn, *Chem. Mater.* **2009**, *21*, 4408.
[23] Y. S. Jung, P. Lu, A. S. Cavanagh, C. Ban, G. H. Kim, S. H. Lee, S. M. George, S. J. Harris, A. C. Dillon, *Adv. Energy Mater.* **2013**, *3*, 213.
[24] J. Qian, L. Liu, J. Yang, S. Li, X. Wang, H. L. Zhuang, Y. Lu, *Nat. Commun.* **2018**, *9*, 4918.
[25] J. Xie, J. Zhao, Y. Liu, H. Wang, C. Liu, T. Wu, P.-C. Hsu, D. Lin, Y. Jin, Y. Cui, *Nano Res.* **2017**, *10*, 3754.
[26] M. Zou, M. Yoshio, S. Gopukumar, J.-i. Yamaki, *Chem. Mater.* **2005**, *17*, 1284.
[27] W. Cho, S. Myeong, N. Kim, S. Lee, Y. Kim, M. Kim, S. J. Kang, N. Park, P. Oh, J. Cho, *Adv. Mater.* **2017**, *29*, 1605578.

**ADVANCED
SCIENCE NEWS**
www.advancedsciencenews.com

**ADVANCED
FUNCTIONAL
MATERIALS**
www.afm-journal.de

[28] Y. Koyama, H. Arai, I. Tanaka, Y. Uchimoto, Z. Ogumi, *Chem. Mater.* **2012**, *24*, 3886.

[29] H. Chen, J. A. Dawson, J. H. Harding, *J. Mater. Chem. A* **2014**, *2*, 7988.

[30] C. A. Marianetti, G. Kotliar, G. Ceder, *Nat. Mater.* **2004**, *3*, 627.

[31] A. Van der Ven, M. K. Aydinol, G. Ceder, *J. Electrochem. Soc.* **1998**, *145*, 2149.

[32] Z. Chen, Z. Lu, J. R. Dahn, *J. Electrochem. Soc.* **2002**, *149*, A1604.

[33] J. M. Paulsen, J. R. Mueller-Neuhaus, J. R. Dahn, *J. Electrochem. Soc.* **2000**, *147*, 508.

[34] A. Yano, M. Shikano, A. Ueda, H. Sakaebe, Z. Ogumi, *J. Electrochem. Soc.* **2017**, *164*, A6116.

[35] J.-H. Shim, J.-M. Han, J.-H. Lee, S. Lee, *ACS Appl. Mater. Interfaces* **2016**, *8*, 12205.

[36] Y. Jin, S. Xu, Z. Li, K. Xu, W. Ding, J. Song, H. Wang, J. Zhao, *J. Electrochem. Soc.* **2018**, *165*, A2267.

[37] R. V. Chebiam, A. M. Kannan, F. Prado, A. Manthiram, *Electrochem. Commun.* **2001**, *3*, 624.

[38] H. Gabrisch, R. Yazami, B. Fultz, *J. Electrochem. Soc.* **2004**, *151*, A891.

[39] W. M. Seong, K. Yoon, M. H. Lee, S.-K. Jung, K. Kang, *Nano Lett.* **2018**, *18*, 8071.

[40] G. Cherkashinin, K. Nikolowski, H. Ehrenberg, S. Jacke, L. Dimesso, W. Jaegermann, *Phys. Chem. Chem. Phys.* **2012**, *14*, 12321.

[41] D. Takamatsu, Y. Koyama, Y. Orikasa, S. Mori, T. Nakatsutsumi, T. Hirano, H. Tanida, H. Arai, Y. Uchimoto, Z. Ogumi, *Angew. Chem., Int. Ed.* **2012**, *51*, 11597.

[42] X. Yu, A. Manthiram, *Energy Environ. Sci.* **2018**, *11*, 527.

[43] F. Lin, D. Nordlund, I. M. Markus, T.-C. Weng, H. L. Xin, M. M. Doeff, *Energy Environ. Sci.* **2014**, *7*, 3077.

[44] S. Myeong, W. Cho, W. Jin, J. Hwang, M. Yoon, Y. Yoo, G. Nam, H. Jang, J.-G. Han, N.-S. Choi, *Nat. Commun.* **2018**, *9*, 3285.

[45] W.-S. Yoon, K.-B. Kim, M.-G. Kim, M.-K. Lee, H.-J. Shin, J.-M. Lee, J.-S. Lee, C.-H. Yo, *J. Phys. Chem. B* **2002**, *106*, 2526.

[46] L. Giordano, P. Karayaylali, Y. Yu, Y. Katayama, F. Maglia, S. Lux, Y. Shao-Horn, *J. Phys. Chem. Lett.* **2017**, *8*, 3881.

[47] S. Sharifi-Asl, J. Lu, K. Amine, R. Shahbazian-Yassar, *Adv. Energy Mater.* **2019**, *9*, 1900551.

[48] M. He, L. Hu, Z. Xue, C. C. Su, P. Redfern, L. A. Curtiss, B. Polzin, A. von Cresce, K. Xu, Z. Zhang, *J. Electrochem. Soc.* **2015**, *162*, A1725.

[49] Z. Zhang, L. Hu, H. Wu, W. Weng, M. Koh, P. C. Redfern, L. A. Curtiss, K. Amine, *Energy Environ. Sci.* **2013**, *6*, 1806.

[50] L. Yang, B. Ravdel, B. L. Lucht, *Electrochem. Solid-State Lett.* **2010**, *13*, A95.

[51] J. L. Tebbe, T. F. Fuerst, C. B. Musgrave, *ACS Appl. Mater. Interfaces* **2016**, *8*, 26664.

[52] J. L. Tebbe, T. F. Fuerst, C. B. Musgrave, *J. Power Sources* **2015**, *297*, 427.

[53] W. Li, A. Dolocan, P. Oh, H. Celio, S. Park, J. Cho, A. Manthiram, *Nat. Commun.* **2017**, *8*, 14589.

[54] K. Edström, T. Gustafsson, J. O. Thomas, *Electrochim. Acta* **2004**, *50*, 397.

[55] M. Gauthier, T. J. Carney, A. Grimaud, L. Giordano, N. Pour, H.-H. Chang, D. P. Fenning, S. F. Lux, O. Paschos, C. Bauer, F. Maglia, S. Lupart, P. Lamp, Y. Shao-Horn, *J. Phys. Chem. Lett.* **2015**, *6*, 4653.

[56] L. Zou, J. Li, Z. Liu, G. Wang, A. Manthiram, C. Wang, *Nat. Comm.* **2019**, *10*, 3447.

**ADVANCED
FUNCTIONAL
MATERIALS**

Supporting Information

Unveiling Nickel Chemistry in Stabilizing High-Voltage Cobalt-Rich Cathodes for Lithium-Ion Batteries

Moonsu Yoon, Yanhao Dong, Youngbin Yoo, Seungjun Myeong, Jaeseong Hwang, Junhyeok Kim, Seong-Hyeon Choi, Jaekyung Sung, Seok Ju Kang, Ju Li,* and Jaephil Cho*

Supporting Information

Unveiling Nickel Chemistry in Stabilizing High-Voltage Cobalt-rich Cathodes for Lithium-Ion Batteries

Moonsu Yoon[1], Yanhao Dong[2], Youngbin Yoo[1], Seungjun Myeong[1,3], Jaeseong Hwang[1], Junhyeok Kim[1], Seong-Hyeon Choi[1], Jaekyung Sung[1], Seok Ju Kang[1], Ju Li[2]* and Jaephil Cho[1]*

[1]Department of Energy Engineering, School of Energy and Chemical Engineering, Ulsan National Institute of Science and Technology (UNIST), 50 UNIST-gil, Ulsan 44919, Republic of Korea

[2]Department of Materials Science and Engineering, Massachusetts Institute of Technology, Cambridge, Massachusetts 02139, United States

[3]Department of Materials, University of Oxford, Parks Road, Oxford OX1 3PH, UK

*Corresponding author: liju@mit.edu, jpcho@unist.ac.kr

Methods

Preparation of LiCoO₂ (LCO) and LiCo₀.₉₅Ni₀.₀₅O₂ (LCNO) : The Co-rich cathode of LCNO was synthesized via a solid-state method using Li_2CO_3, Co_3O_4 and $Ni(OH)_2$ as precursors with a molar ratio of Li:Co:Ni = 1.015:0.95:0.05. The starting materials were mixed by a mechanical mixer at 2,000 rpm. The prepared powder was annealed at 450 °C for 30 min (heating rate of 2.83 °C min^{-1}), followed by sintering at 970 °C for 7 h (heating rate of 1.79 °C min^{-1}) under the ambient air. Commercial LCO was purchased from Cosmo AM&T (Republic of Korea) and used without any further modification.

Material characterization: Particle size distribution was measured by the Fraunhofer approximation by laser diffraction particle size analysis instrument (Microtrac S3500, Microtrac). Specific surface area was estimated with the BET theory with porosity and surface area analyzer (TriStar II, micromeritics). Chemical compositions of both cathode material and dissolved transition metal in electrolyte were determined by an inductively coupled plasma optical emission spectrometer (ICP-OES, Varian 700-ES, Varian, Inc.) The crystallographic structure of each LCO and LCNO was investigated by X-ray diffraction (XRD) using a parallel beam XRD instrument (Smartlab, $\lambda_{CuK\alpha}$=1.542 Å, Rigaku). A scan range was from 10° to 80° (2 theta) with a scan step of 0.02° and a counting time of 5 s. The morphology of the cathode powder and the electrode surface were analyzed by scanning electron microscopy (SEM, Verios 460, FEI) with energy dispersive X-ray spectroscopy (EDX, XFlash® 6130, Bruker) detector.

   Cross-sectional images of the cathode particles were obtained by dual-beam focused ion beam (FIB, Helios 450HP, FEI). For analyzing surface microstructure of the cathode particle, the crosssectioned samples were further thinned by Ar-ion milling system (Model 1040 Nanomill, Fischione). After this treatment, high-resolution transmission electron microscopy (HR-TEM, ARM300, JEOL) operating at 150 keV and 300 keV was utilized to collect scanning transmission electron microscopy (STEM) imaging of the samples for an atomic and structural analysis. For elemental and electronic analysis, the

energy dispersive X-ray spectroscopy (EDX) and electron energy loss spectroscopy (EELS) were conducted by using the same HR-TEM attached EDX (Aztec, Oxford).

Electrode surface chemistry was analyzed using X-ray photon spectroscopy (XPS, Thermo Scientific Kα spectrometer). For the time-of-flight secondary-ion mass spectrometry (TOF-SIMS) studies, TOF-SIMS 5 spectrometer (ION-TOF GmbH) was used under the pressure of analysis chamber below 5.0×10^{-10} torr. All detected secondary ions of interest had a mass resolution > 10,000 and possessed negative polarity. The Burst Alignment mode with pulsed 30 keV Bi_1^+ (20 ns) ion beam was applied for high lateral resolution mapping (< 200 nm) analysis, and typical analysis area was 100 × 100 µm. TOF-SIMS mapping and spectra of secondary ions of interest were collected after 100 s of Cs^+ ion beam sputtering. Before the XPS and TOF-SIMS measurements, all samples were rinsed in dimethyl carbonate and dried in an argon-filled glovebox, and then transferred to the instruments.

Cell fabrication and electrochemical measurements. Electrochemical performances were evaluated with 2032R coin type half-cell and pouch type full-cell. First, each LCO and LCNO composite electrode was prepared for the half-cell test by blending 91 wt% cathode active material, 5 wt% Super-P (as a conductive agent), and 4 wt% poly(vinylidene fluoride) binder, dissolved in N-methyl-2-pyrrolidone (NMP). The resulting slurry was coated onto aluminum foil and then dried at 120 °C for 2 h. The loading level of the electrode was controlled to ~15.2 (±0.1) mg cm^{-2}, and all the electrodes were pressed with an electrode density of ~4.0 (±0.05) g cm^{-3}. These cathode electrodes were fabricated into coin type half-cells in an argon-filled glove box with Li metal as a negative electrode. A solution of 1 M LiPF$_6$ in ethylene carbonate (EC), dimethyl carbonate (DMC), and diethyl carbonate (DEC) (1:2:1, v/v/v) (Panax Etec.) was used for the electrolyte. All cathode half-cells were evaluated with constant current (CC)–constant voltage (CV) mode between 3.0 and 4.45 V (vs. Li/Li$^+$) at 25 °C. The initial charge-discharge cycle was performed on the assembled cells at a C-rate of 0.1C, and then these were tested with a constant current of 1.0C charge and 1.0 C discharge. The rate capability test was

3

performed at a 0.2 C charge rate and different discharge C-rates of 0.2/0.5/1.0/2.0/3.0/5.0 C. For the differential electrochemical mass spectrometry (DEMS) measurement, the authors used Swagelok type cell design and assembled in the argon glove box. The details of DEMS system are described elsewhere.[1]

The electrochemical floating test was conducted in half-cell configuration with LCNO (or LCO) as the cathode and Li metal as the anode. The effective electrode area was 1.54 cm^2. The LCNO (or LCO)/Li half-cell was charged to 4.45 (or 4.5, 4.6 and 4.7) V at a rate of 0.2C and then maintained at each specific voltage for 27 h (or 5 h) with the current monitored by a TOSCAT-3100 battery cycler (TOYO SYSTEM).

All the electrochemical impedance spectroscopy (EIS) results were obtained from VMP-300 potentiostat (Bio-logic) with frequency range from 1 MHz to 10 MHz and a DC voltage amplitude of 10 mV after fully charged to 4.45 V. The galvanostatic intermittent titration technique (GITT) was employed using coin half cells, cycled in the voltage range of 3.0-4.45 V at a constant charge and discharge rate of 0.5 C for 8 min with a rest time of 1 h. Differential capacity versus voltage (dQ/dV) curves were collected at 0.1 C. Anode composite electrodes were made by mixing 96 wt% spherical graphite powder (S360), 1 wt% Super-P, 1.5 wt% carboxymethyl cellulose (CMC), and 1.5 wt% styrene-butadiene rubber (SBR). The mixed slurry was cast onto copper foil, with a loading level of ~7.15 mg cm^{-2} and dried at 80 °C over 1 h. The coated electrodes were pressed to ~1.65 g cm^{-3}, then dried again in the vacuum oven at 150 °C for 6 h. The obtained anode electrode and Li metal were used to assemble the coin type half-cell, and the cells were tested with voltage varied from 0.005 to 1.5 V (charge and discharge C-rates were 0.5 C and 0.5 C, respectively). All electrochemical tests were carried out using a TOSCAT-3100 battery cycler (TOYO SYSTEM).

For the full-cell test, the loading level and electrode density of cathode electrode were adjusted to ~13.60 (±0.1) mg cm^{-2} and ~4.0 (±0.05) g cm^{-3}, respectively, and the values of the anode electrode

4

were same with those of half-cell. The same electrolyte with the half-cell of cathode and anode was employed in the full-cell test. The N/P ratio of the full-cell was ~1.10. All full-cells were assembled in a pouch type cell and were evaluated with CC–CV mode between 2.7 and 4.35 V. First charge and discharge cycle test were performed with charge and discharge C-rate of 0.1 C. We charged the full-cells to 3.6 V during first charging process to eliminate the generated gaseous product (degassing process) in the full-cell. The cycle performance at 25°C and 45 °C were cycled from 2.7 to 4.35 V with a charge and discharge C-rate of 1C.

First-principles calculations.

All calculations were performed by the Vienna *ab initio* simulation package (VASP) based on density functional theory (DFT) using projector augmented-wave (PAW) method with Perdew-Burke-Ernzerhof (PBE) generalized gradient approximation (GGA). [2-4] PAW potentials with $2s^1$ electron for Li, $3d^7 4s^2$ electrons for Co, $3d^8 4s^2$ electrons for Ni, and $2s^2 2p^4$ electrons for O were used. DFT+U approach[5] was used to describe $3d$ orbitals of Co (U=3.4 eV and J=0 eV) and Ni (U=6.0 eV and J=0) eV. A plane-wave cutoff energy of 520 eV was used and the Brillouin zone was sampled using Monhorst-Pack scheme with a $3\times3\times3$ k-point mesh. The convergence was set reached when residue atomic forces were less than 0.05 eV/Å.

For $LiCoO_2$, a $3\times3\times3$ supercell containing 27 Li, 27 Co and 54 O was used. For Ni doped $LiCoO_2$, we considered two models: (1) $LiNi_{0.074}Co_{0.926}O_2$ close to experimental bulk doping concentration (5 mol% of total transition metal), using a supercell containing 27 Li, 2Ni, 25 Co and 54 O; here the 2 Ni were placed in transition metal layer (substituting Co). (2) $Li_{0.778}Ni_{0.296}Co_{0.926}O_2$ to simulate cation-mixed surface structure of Ni doped $LiCoO_2$ observed experimentally, using a supercell containing 21 Li, 8Ni, 25 Co and 54 O; here 2 Ni were placed in transition metal layer (substituting Co) and 6 Ni were in Li layer (substituting Li). To simulate the delithiated structures of $LiCoO_2$, $LiNi_{0.074}Co_{0.926}O_2$, and $Li_{0.778}Ni_{0.296}Co_{0.926}O_2$, we first removed 18 Li from the supercell of each composition (corresponding

to a capacity around 180 mAh g^{-1}), relaxed the structures at 0 K, then annealed them by first-principles molecular dynamics at 800 K for 1.5 ps with step-like cooling at 600 K, 400 K and 200 K each for 1.5 ps, and finally relaxed the structures again at 0 K. All atomic structures were virtualized using VESTA.
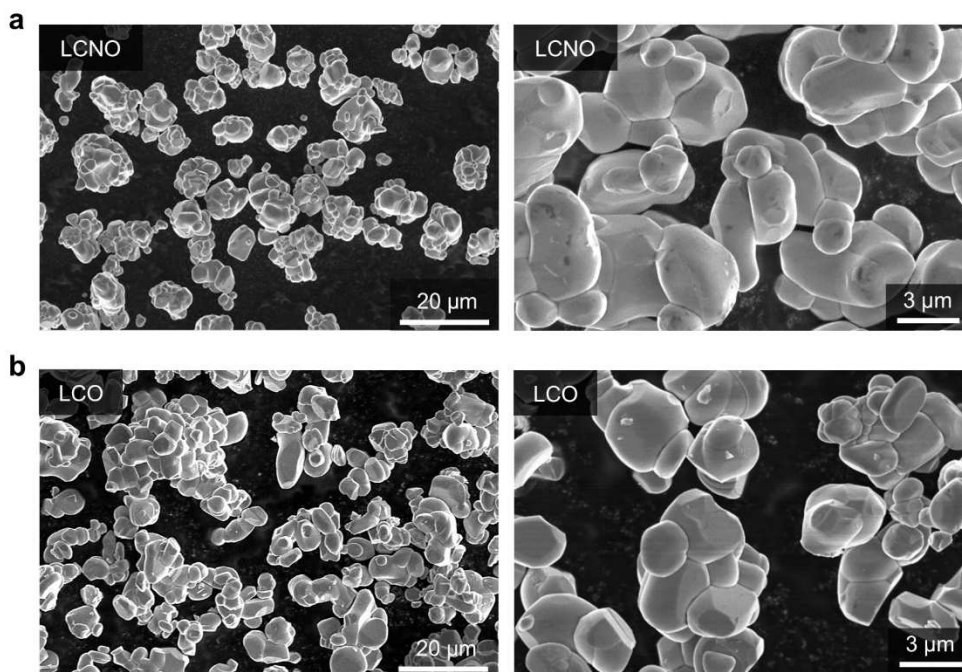
[6]

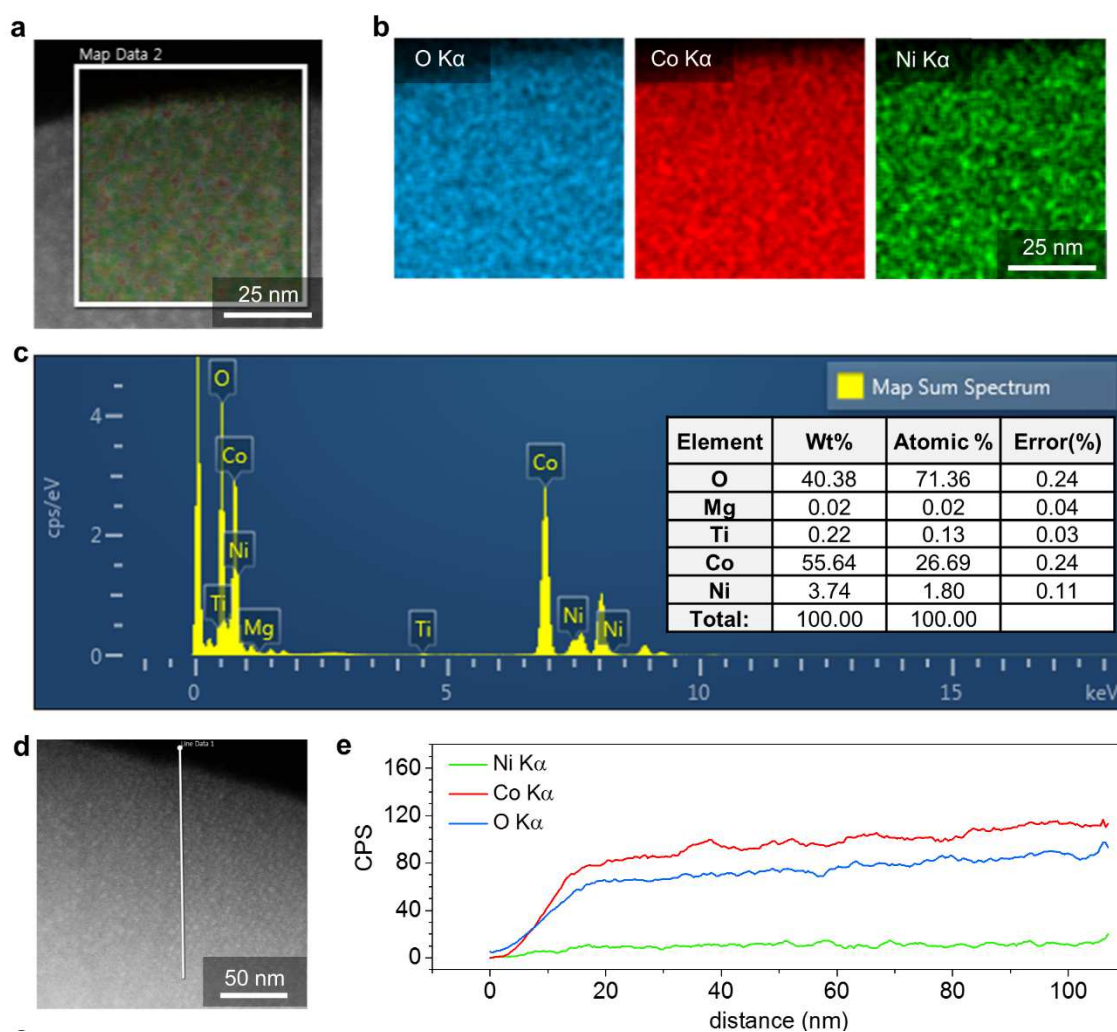Figure S1. Scanning electron microscopy (SEM) images of pristine (a) LCNO and (b) LCO.

Element	Wt%	Atomic %	Error(%)
O	40.38	71.36	0.24
Mg	0.02	0.02	0.04
Ti	0.22	0.13	0.03
Co	55.64	26.69	0.24
Ni	3.74	1.80	0.11
Total:	100.00	100.00	

Figure S2. (a) A magnified cross-sectional transmission electron microscopy (TEM) image of the pristine LCNO particle. (b) Mapping results, showing O Kα, Co Kα and Ni Kα, measured from the selected area in a. (c) Energy dispersive X-ray spectroscopy (EDX)-TEM spectra of pristine LCNO at b, revealing the stoichiometric coherence with target composition of LCNO. (d) The TEM image of cross-sectional LCNO particle with an arrow indicating the EDX line scan position, and (e) the line profiles with O Kα, Co Kα and Ni Kα signal corresponding to the scan line in d.
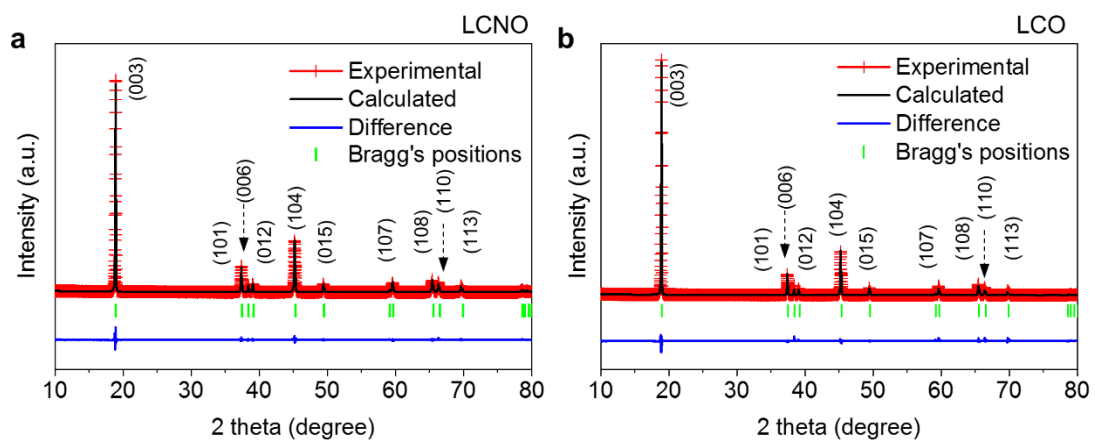
Figure S3. (a) Rietveld refinement of ex situ X-ray diffraction (XRD) patterns for pristine (a) LCNO and (b) LCO powder.
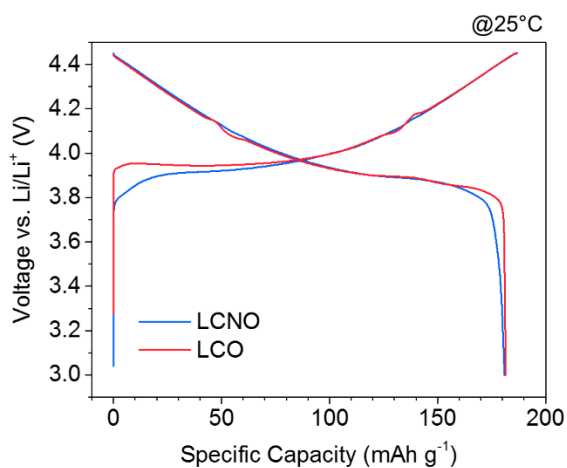
Type	Charge capacity (mAh g^{-1})	Discharge capacity (mAh g^{-1})	Initial coulombic efficiency (%)
LCNO	186.8	180.9	96.8
LCO	186.3	181.5	97.4

Figure S4. Initial charge-discharge profiles (formation cycle) of the LCNO and LCO at 0.1C rate with a voltage ranged from 3.0 to 4.45V at 25°C.
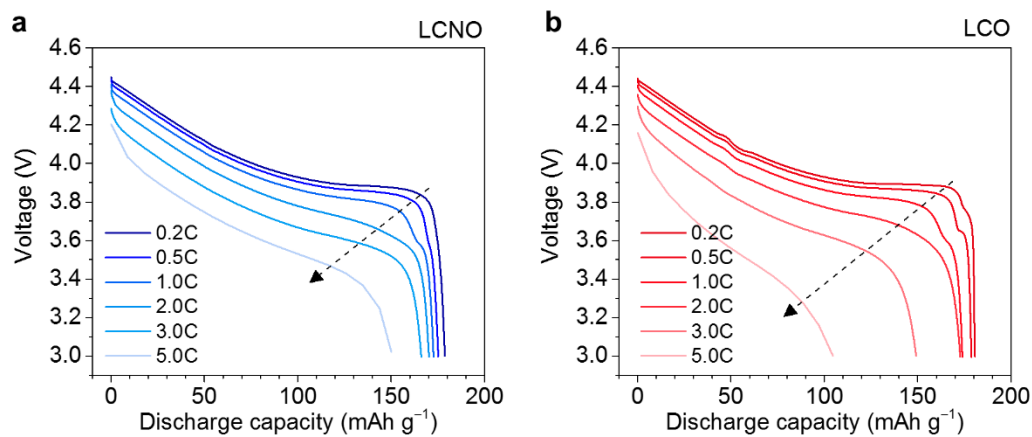
Figure S5. Rate performance of (a) LCNO and (b) LCO at 25°C where the operating voltage ranged from 3.0–4.45 V. The discharge C-rate increased from 0.2 to 5C with a fixed charge rate of 0.5C.

10
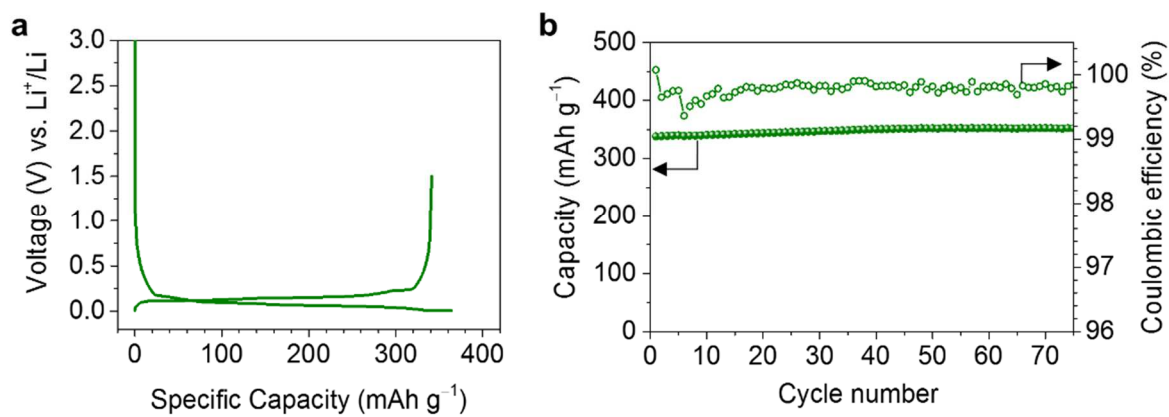
Figure S6. (a) Initial charge-discharge voltage profile of the spherical graphite (Gr) at 25°C (CC-CV mode, charge and discharge C-rate: 0.1 and 0.1C). (b) Cycle performance of the Gr at the voltage range of 0.005–1.5 V (vs. Li/Li$^+$) with charge and discharge C-rate of 0.5 and 1.0C, respectively.
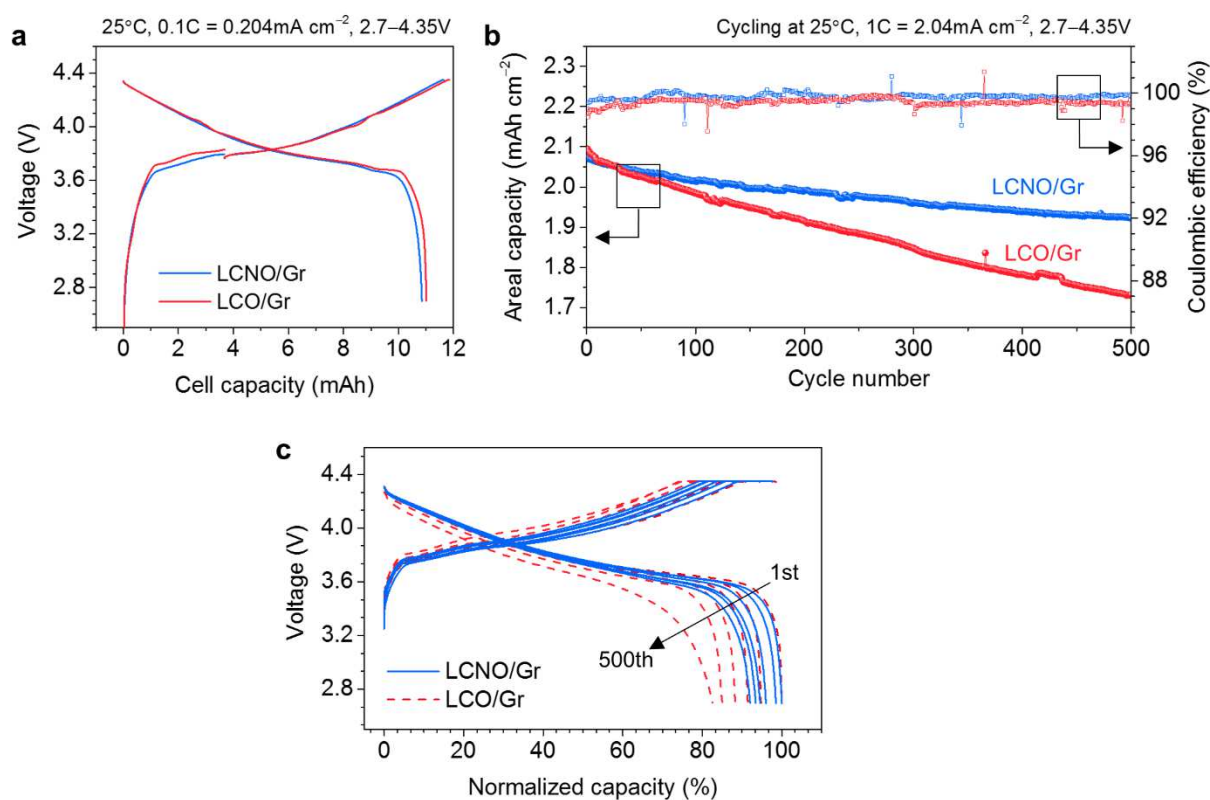
Figure S7. Electrochemical properties of the LCNO/Gr and LCO/Gr full-cell at 25°C. (a) Initial full-cell formation step of the LCNO/Gr and LCO/Gr, which was performed at 2.7–4.35V with a charge and discharge C-rate of 0.1C. (b) Cycle performance of the LCNO/Gr and LCO/Gr full-cells (galvanostatic charge-discharge cycling was performed with a charge and discharge C-rate of 1.0C≈2.04 mA cm^{-2}). (c) Normalized voltage profiles of each LCNO/Gr and LCO/Gr full-cell collected from 1st, 100th, 200th, 300th, 400th and 500th cycle.
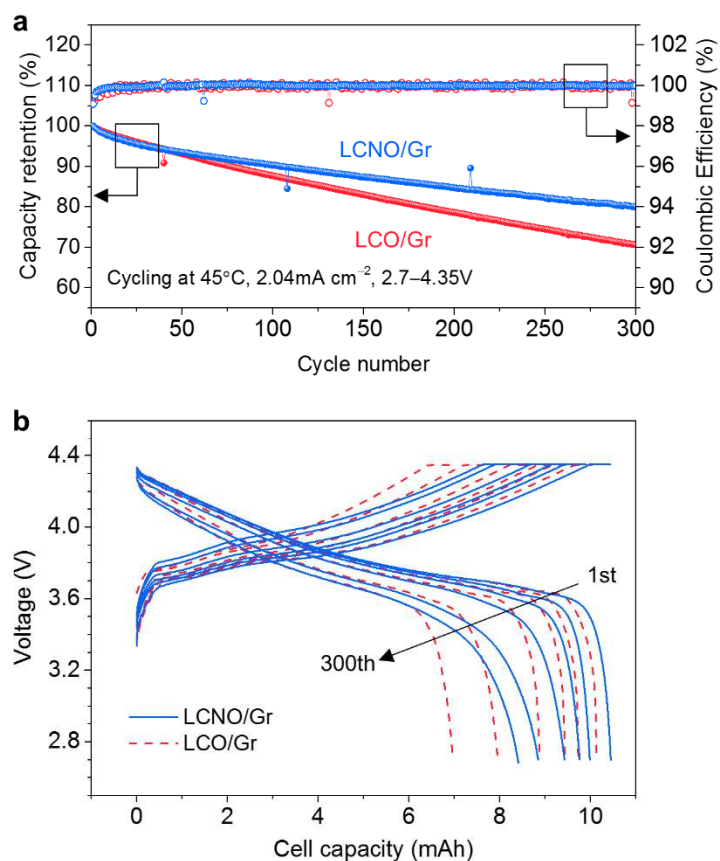
Figure S8. Electrochemical properties of each LCNO/Gr and LCO/Gr full-cell at 45 °C. (a) Cycle performance of the LCNO/Gr and LCO/Gr full-cells at 45°C (galvanostatic charge-discharge cycling was performed at 2.7–4.35V with a charge and discharge C-rate of $1.0C \approx 2.04$ mA cm^{-2}). (c) Voltage profiles of the LCNO/Gr and LCO/Gr full-cells collected from 1st, 25th, 50th, 100th, 200th and 300th cycle.
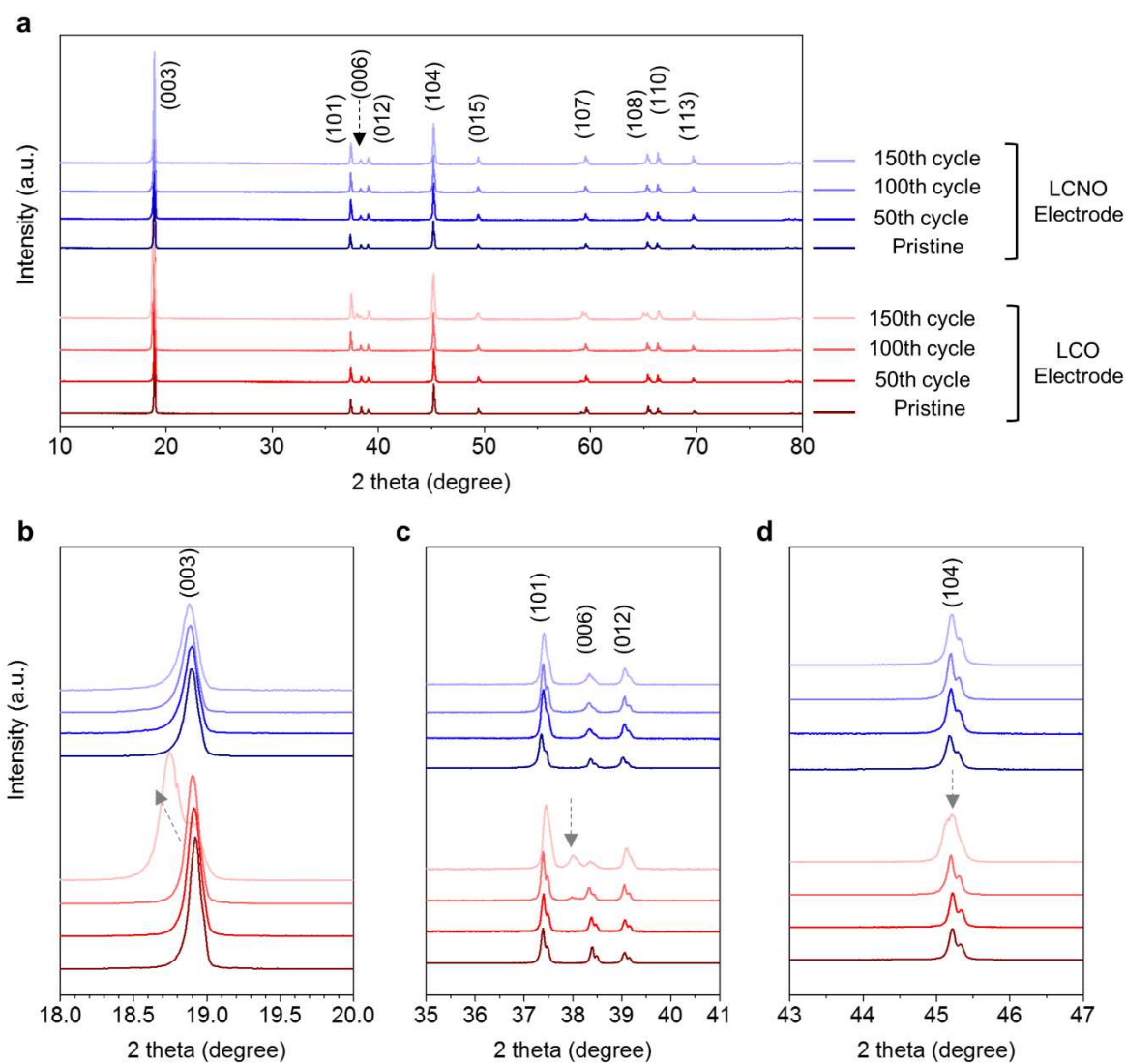
Figure S9. (a) *Ex situ* XRD patterns of the pristine, 50th, 100th and 150th cycled electrodes of LCNO and LCO. (b-d) Magnified XRD patterns of (a), illustrating the dramatic shift of the (003) reflection and fading of the (006) reflection. These results imply that the bulk phase transformation in LCO occurs at least after 100 cycles.
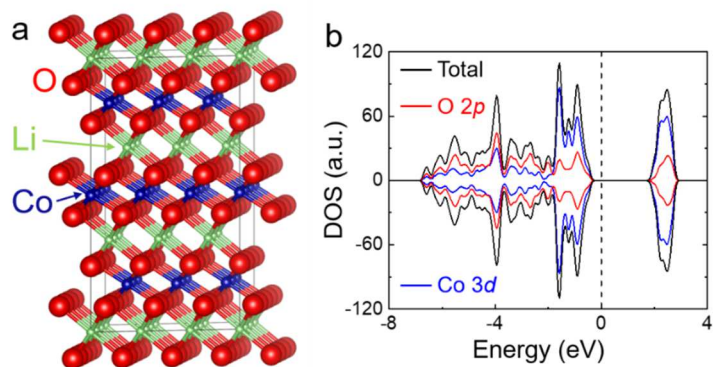
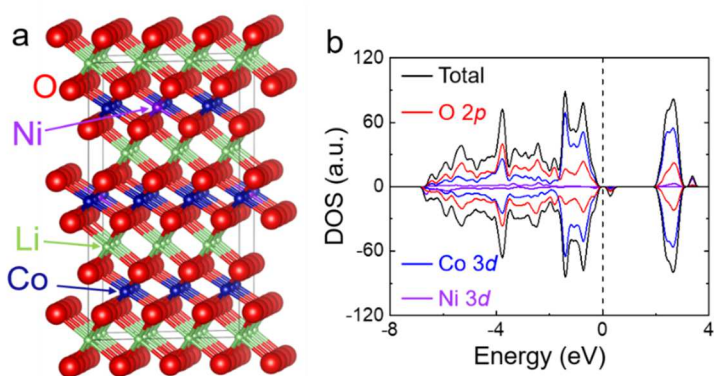Figure S10. (a) Atomic structure and (b) density of states of stoichiometric LiCoO$_2$.

Figure S11. (a) Atomic structure and (b) density of states of stoichiometric LiNi$_{0.074}$Co$_{0.926}$O$_2$.

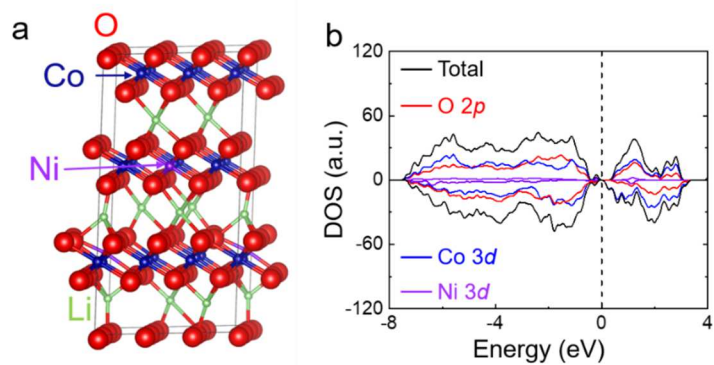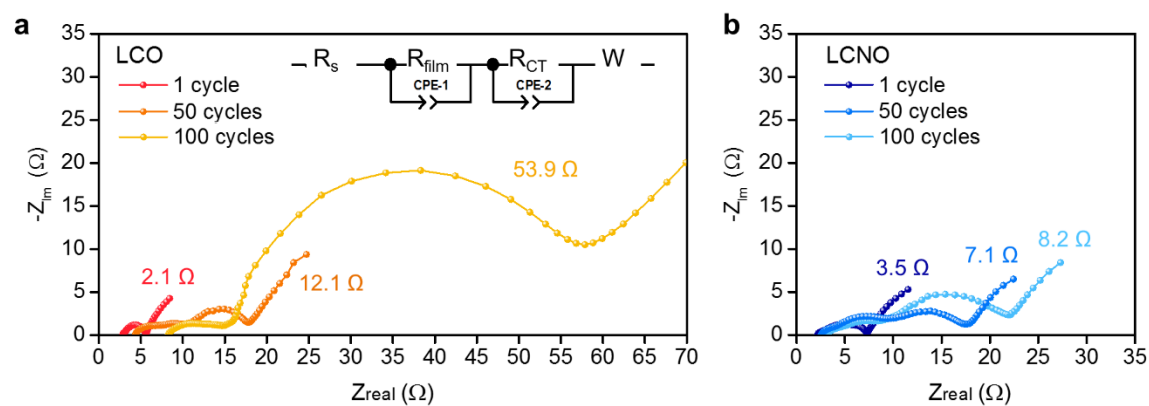Figure S12. (a) Atomic structure and (b) density of states of delithiated Li$_{0.333}$Ni$_{0.074}$Co$_{0.926}$O$_2$.

	1st cycle			50th cycle			100th cycle	
Sample	LCO	LCNO	Sample	LCO	LCNO	Sample	LCO	LCNO
R_s (Ω)	2.6	2.1	R_s (Ω)	4.1	2.1	R_s (Ω)	7.8	2.8
R_{film} (Ω)	1.5	2.2	R_{film} (Ω)	6.8	4.1	R_{film} (Ω)	16.8	4.2
R_{CT} (Ω)	2.1	3.5	R_{CT} (Ω)	12.1	7.1	R_{CT} (Ω)	53.9	8.2

Figure S13. Electrochemical impedance spectroscopy (EIS) results of the half-cell with each (a) LCO and (b) LCNO cathode measured at 1st, 50th, and 100th cycle. The inset diagram in (a) is an equivalent circuit corresponding to this half-cell. Resistances from the fitted equivalent circuit of experimental data for LCO and LCNO corresponding to each 1st ,50th ,and 100th cycle.
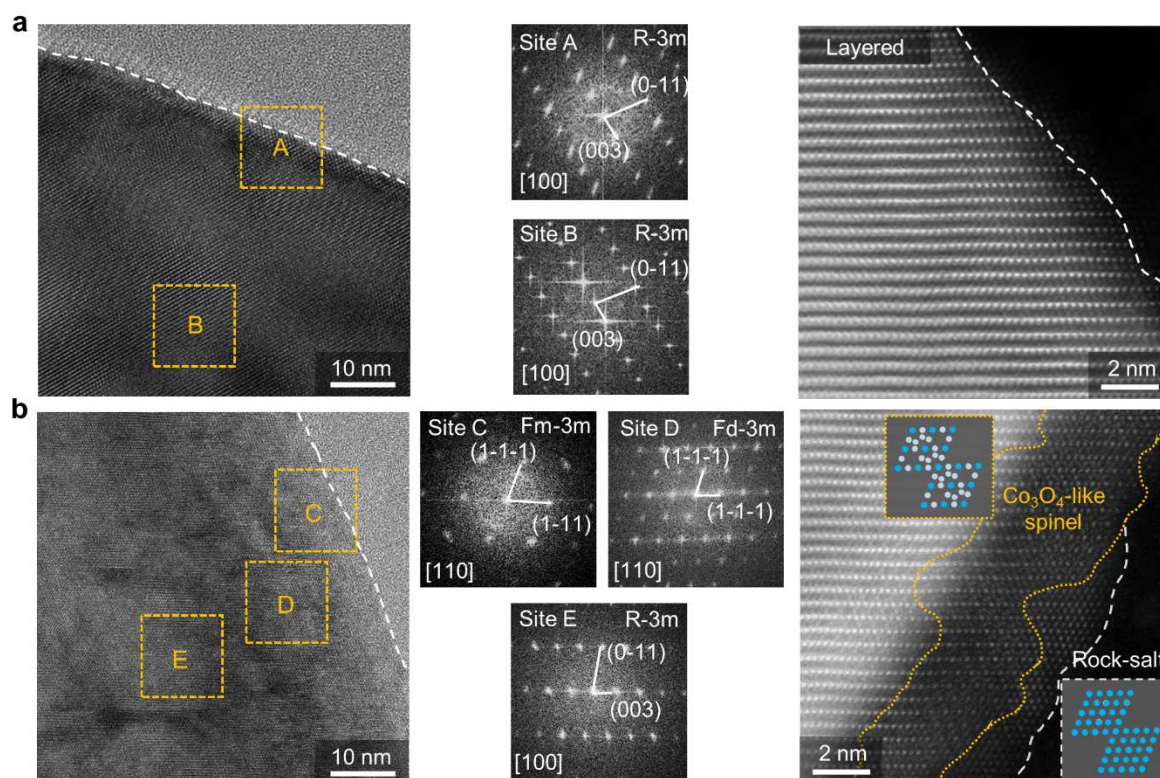
Figure S14. Structural information of pristine LCO and 100th-cycled LCO (a) Pristine LCO overall consists of the layered structure with R$\bar{3}$m phase, showing its corresponding fast Fourier transform (FFT) patterns as inset (middle) throughout a specimen. The magnified high-angle annular dark-field (HAADF)-STEM image of pristine LCO (right). (b) The High resolution-TEM with corresponding local FFT patterns and magnified HAADF-STEM images collected from different region within 100th-cycled LCO. The corresponding FFT patterns from regions marked by dashed square with C, D and E demonstrate Fm$\bar{3}$m (rocksalt), Fd$\bar{3}$m (spinel), and R$\bar{3}$m (layered) phase in an order from the outer surface, and the magnified HAADF-STEM image of cycled LCO clearly shows the different local phase evolution after cycling.
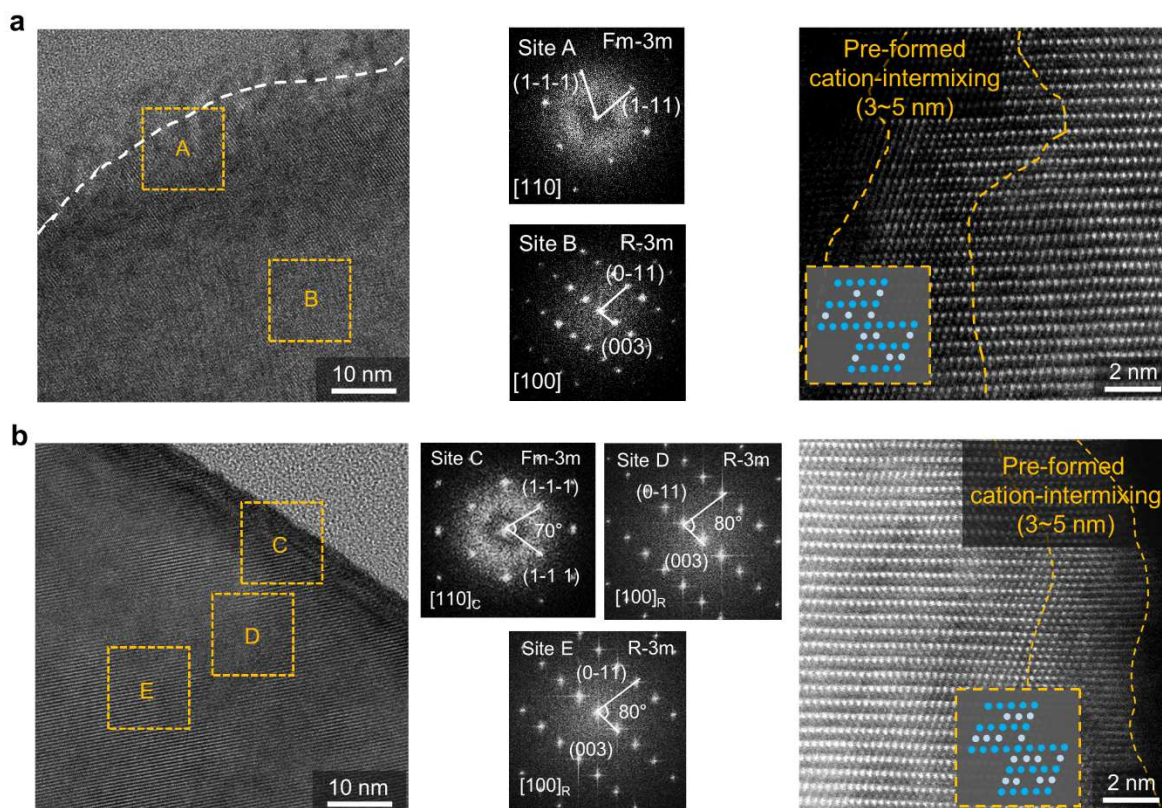
17

Figure S15. Structural information of pristine LCNO and 100th-cycled LCNO. (a) Pristine LCNO mostly consists of the layered structure ($R\overline{3}m$), and the thin pre-formed cation-mixed structure layer with low intensity is narrowly distributed along its outer surface region (3~4nm). The pre-formed cation-intermixing layer differentiates LCNO from LCO. (b) The high resolution-TEM with corresponding local FFT patterns and magnified HAADF-STEM images collected from different region within 100th-cycled LCNO. These results clearly suggest the surface structure integrity of cycled LCNO was well preserved even after 100 cycles.
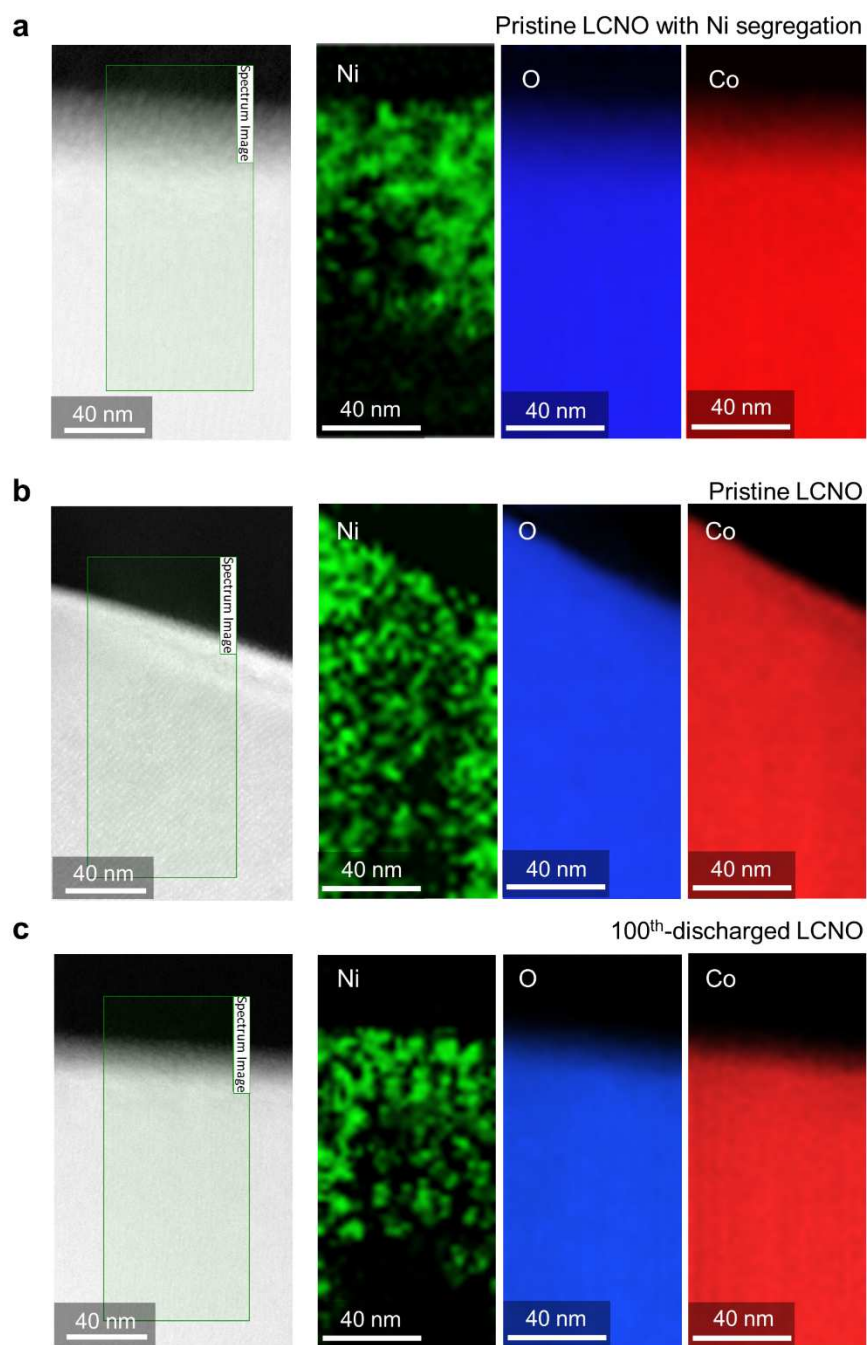
Figure S16. (a-c) TEM-EELS mapping results of pristine and 100th-dishcarged LCNO. Note: For pristine LCNO, 13 local regions close to the surface were measured, among which 6 local regions clearly show Ni surface segregation (one example shown in a) and the other 7 do not show strong segregation (one example shown in b). In 100th-discharged LCNO, 5 local regions close to the surface were measured, among which 4 local regions show strong Ni segregation (one example shown in c).
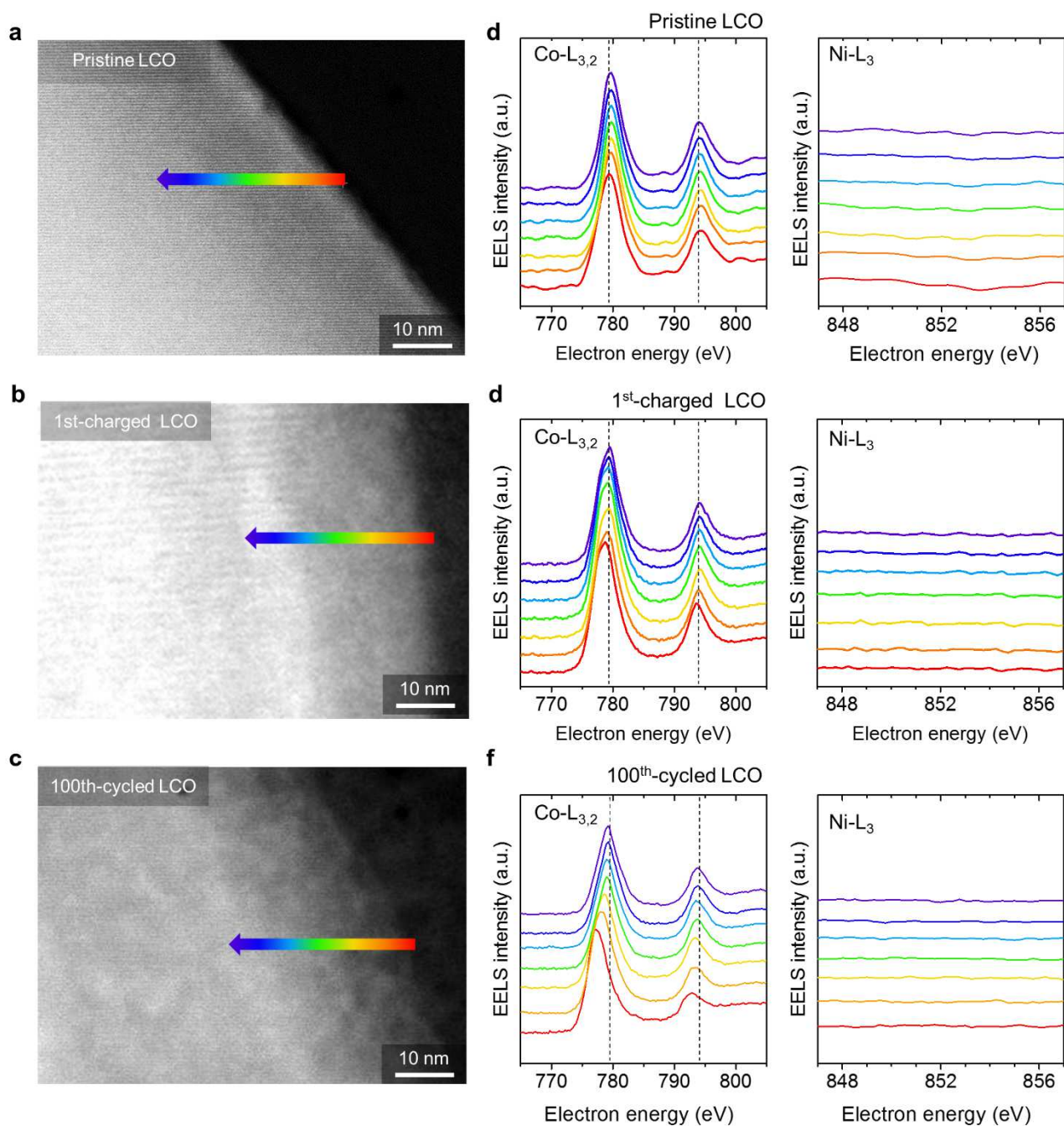
Figure S17. (a-c) Low magnification HAADF-STEM images of LCO with a rainbow-colored arrow for EELS line profiling at different states (pristine, 1st-charged and 100th-cycled). (d-f) Co-L and Ni-L edge EELS spectra measured at different state of LCO (pristine, 1st-charged and 100th-cycled) along the scanning pathway, shown in (a-c), respectively. The spectra were calibrated by setting the highest intensity of the O-K edge due to the lack of the calibration of zero loss peak.

Figure S18. (a-c) Low magnification HAADF–STEM images of LCNO with a rainbow-colored arrow for EELS line profiling at different states (pristine, 1st-charged and 100th-cycled). (d-f) Co-L and Ni-L edge EELS spectra measured at different state of LCNO (pristine, 1st-charged and 100th-cycled) along the scanning pathway, shown in (a-c), respectively. The spectra were calibrated by setting the highest intensity of the O-K edge due to the lack of the calibration of zero loss peak.
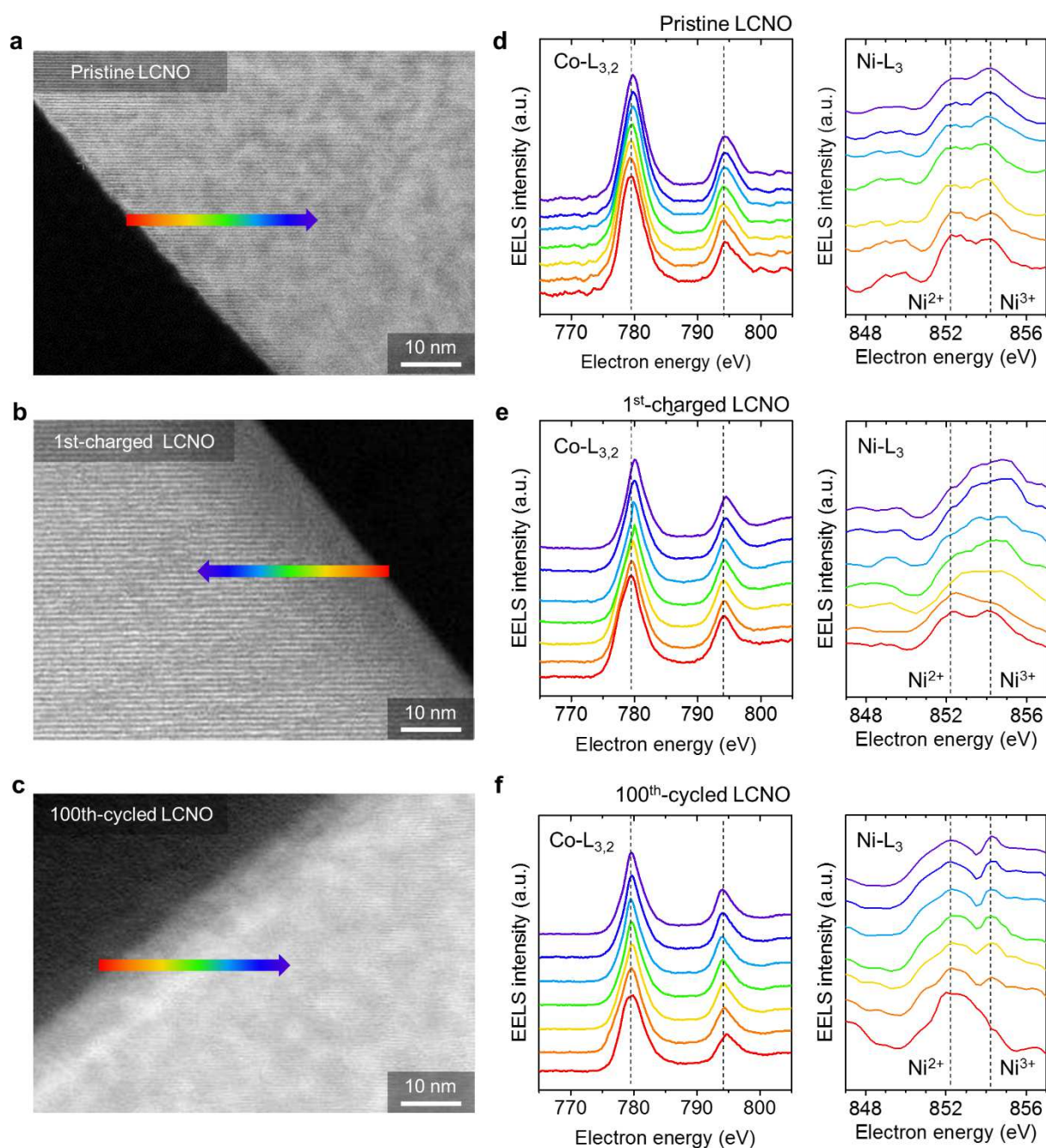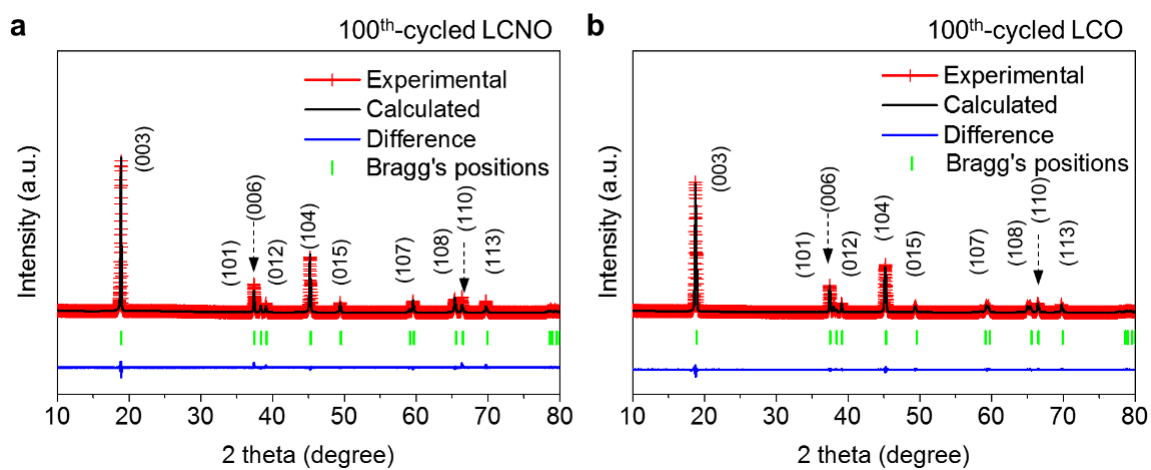
Figure S19. Rietveld refinement of XRD patterns for 100th-cycled (a) LCNO and (b) LCO.

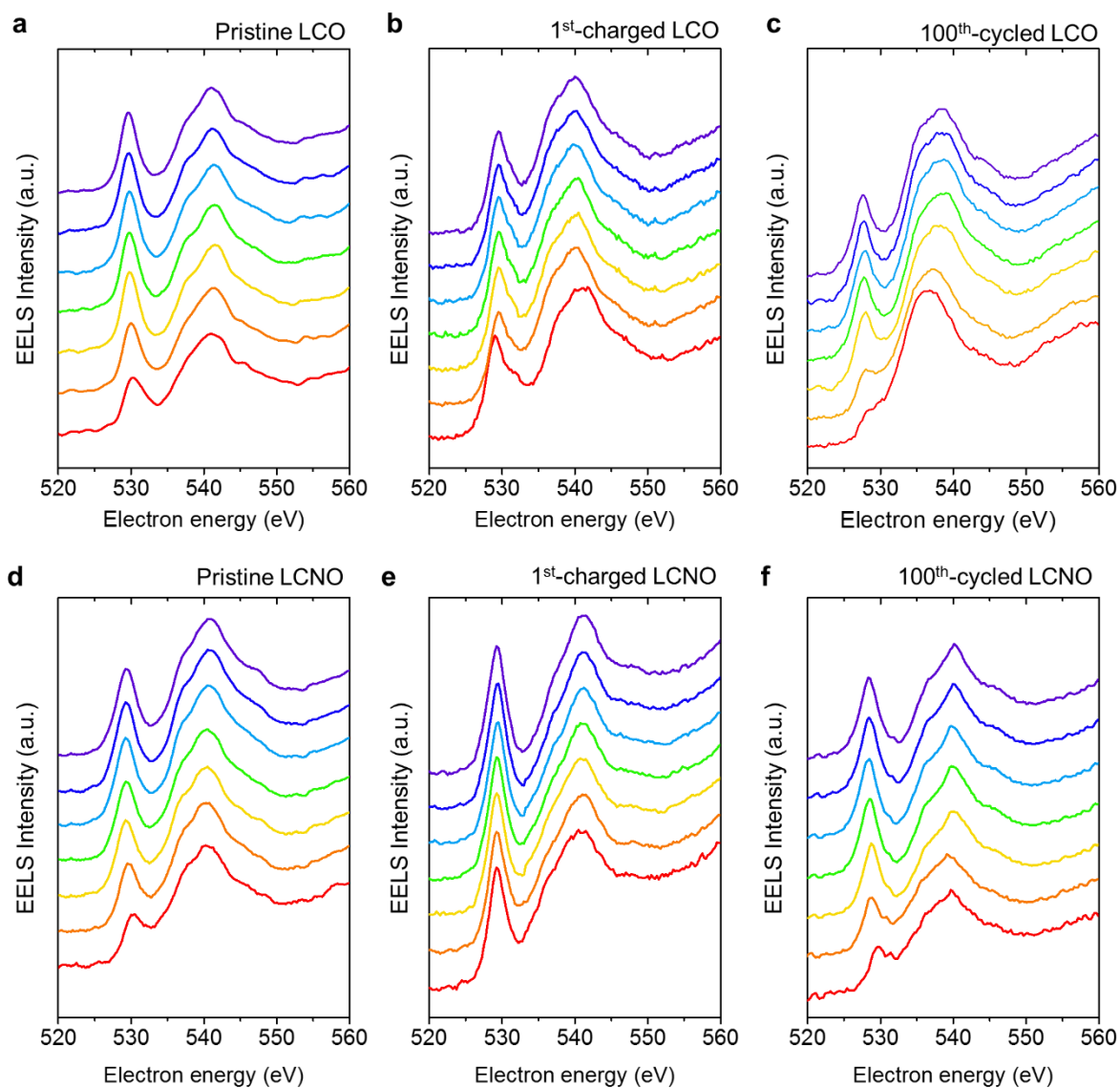Figure S20. (a-c) EELS O K edge spectra for LCO, measured at each different state (pristine, 1st-charged and 100th-cycled). (d-f) EELS O K edge spectra for LCNO, measured at each different state (pristine, 1st-charged and 100th-cycled). The scanning pathways for EELS spectra are suggested in Figure S17 (a-c) and Figure S18 (a-c), respectively. The spectra were normalized to the strongest signal around ~540 eV.
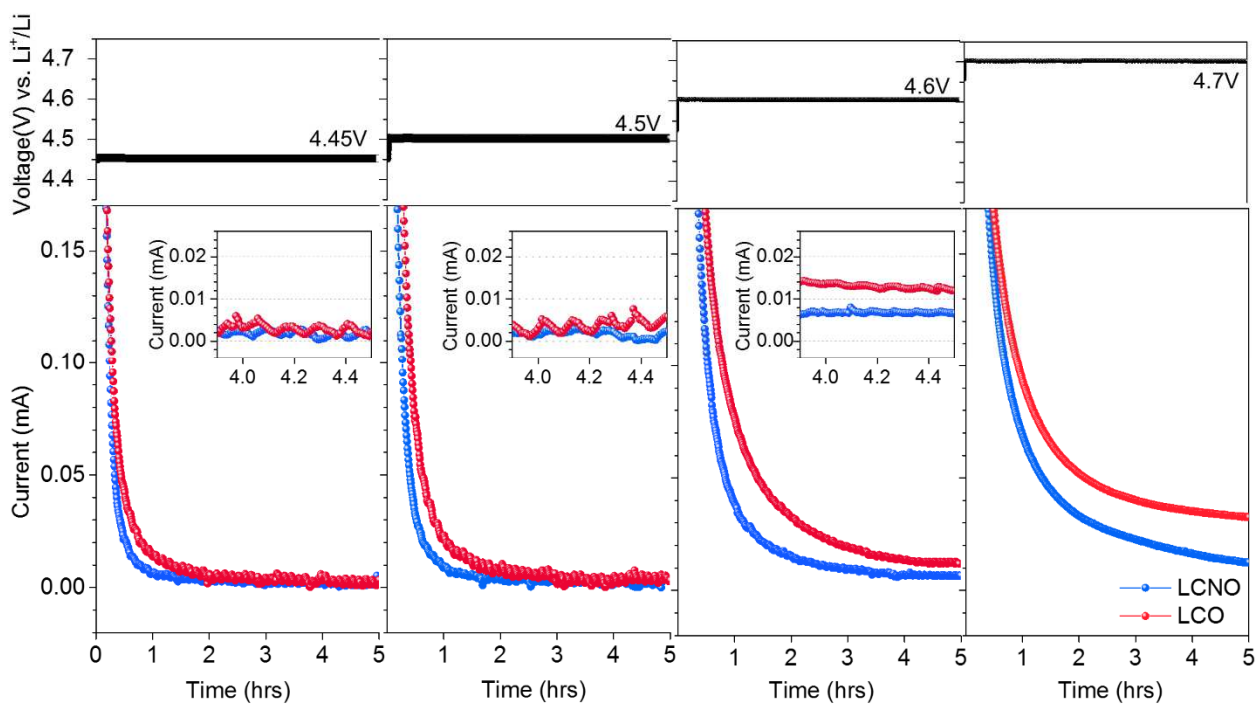
Figure S21. Floating test results of LCNO and LCO at each different constant voltage mode of 4.45, 4.5, 4.6 and 4.7 V(vs. Li$^+$/Li), respectively, in early 5 hours.
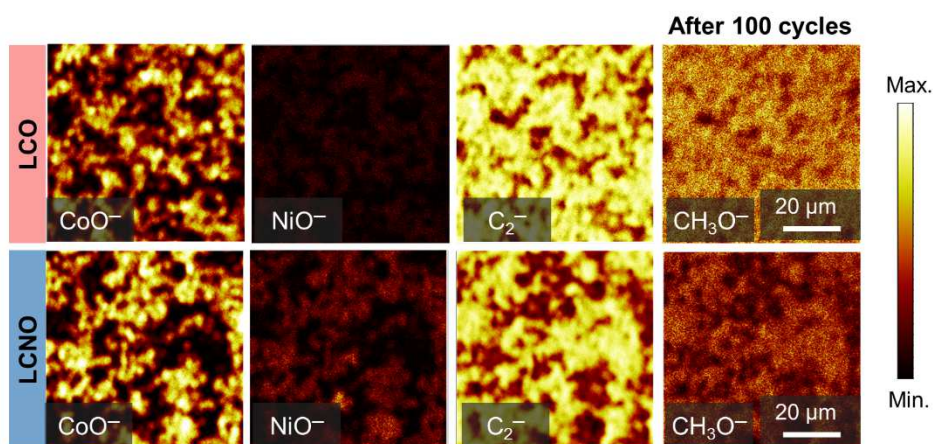
Figure S22. Comparison of time-of-flight secondary-ion mass spectrometry (TOF-SIMS) mappings (burst alignment mode) for the cycled LCO and LCNO electrodes. The shown images are top views of each electrode collected after 100s Cs^+ sputtering. From the left to right, the secondary ions of interest are, respectively, CoO^-, NiO^-, C_2^- and CH_3O^-. Notably, carbonate-based electrolyte decomposition product is less accumulated on conductive agent/binder region (represented by C_2^-) of LCNO electrode compared to that of LCO electrode. It is reasonably presumed that lots of organic interphasial chemistry (represented by CH_3O^-) at the conducting agent/binder region of LCO electrode are the collateral damage from dynamic communication between the active cathode material and conductive carbon/binder, as previously discussed by Li et al.[7]
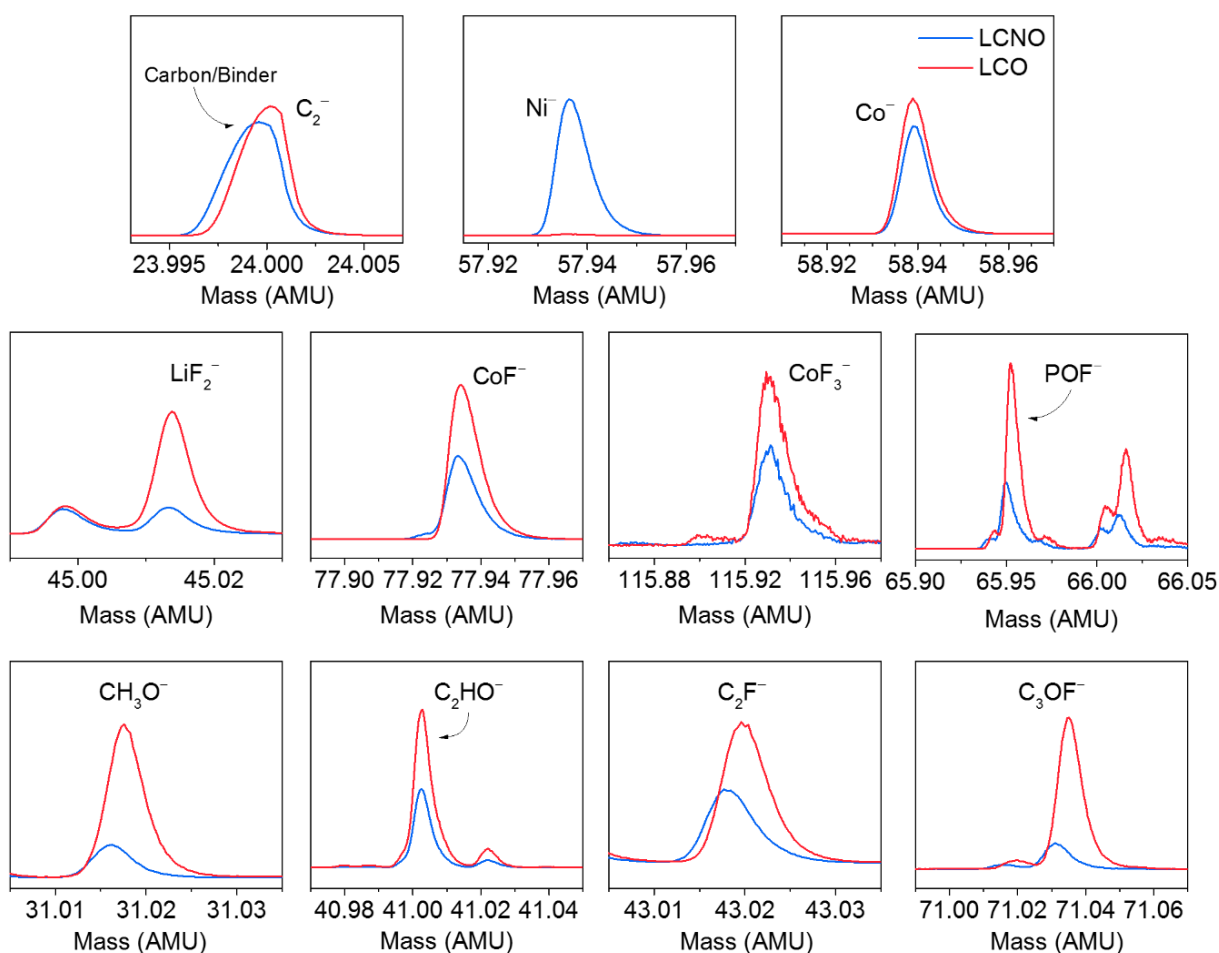
Figure S23. TOF-SIMS spectra of several fragments representing the basic electrode component (top row), fluoride compound (middle row) and carbonate-based electrolyte decomposition products (bottom row) on LCNO and LCO electrodes after 100 cycles at 25°C. All spectra data was integrated over 100s Cs^+ sputtering and sputtering time with two scans per 10s. It can be seen that the side reaction products, from decomposed carbonated-based solvent and HF species[8, 9], were severely accumulated on the surface of LCO electrode during the high-voltage battery operation, and the active mass dissolution was also much more aggravated on LCO electrode than on LCNO electrode.

Figure S24. (a-d) SEM images and EDX mapping results of the LCNO and LCO (the state and type of samples are depicted in the upper left of SEM images). Compared to (a-c), the SEM image of LCO after 1st floating test (d) shows large amount of impurit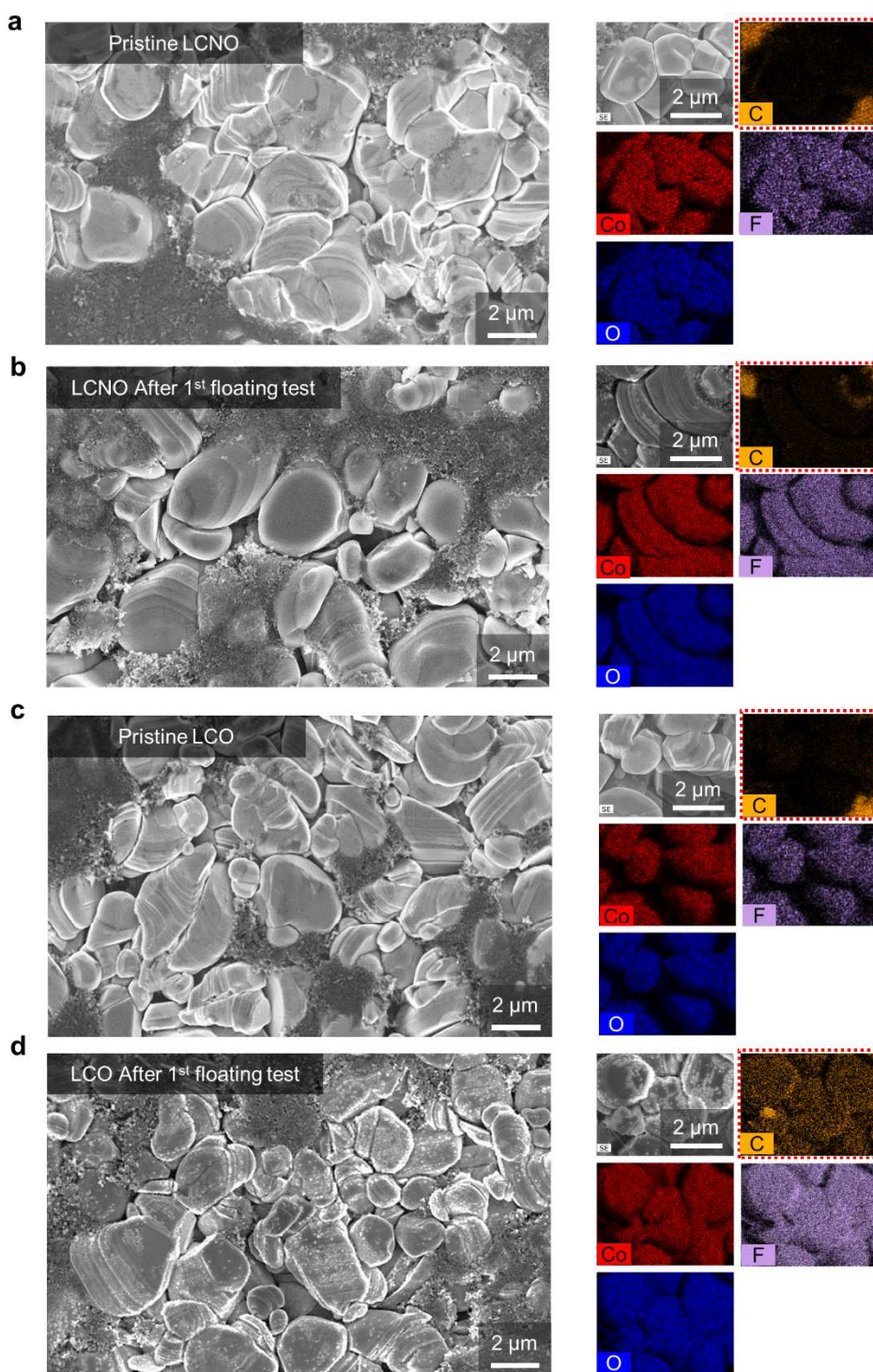ies accumulated on the surface. In EDX mapping of the cycled LCO, illustrative map of carbon (C) depicts the interphase on the surface of active material.

27

Supplementary Table

Table S1. Size distribution and surface area of LCNO and LCO particles.

Sample	Particle size distribution			BET $(m^2\ g^{-1})$
	D_{10}	D_{50}	D_{90}	
LCO	7.42	10.02	17.86	0.3445
LCNO	7.83	10.42	18.85	0.3425

Table S2. Inductively coupled plasma-optical emission spectrometry (ICP-OES) analysis results of pristine state of LCNO and LCO powder.

Type	Mol(%)						
	Li/Metal	Ni/Metal	Co/Metal	Mn/Metal	Mg/metal	Ti/Metal	Al/Metal
LCNO	100.4%	4.884%	94.751%	0.000%	0.238%	0.135%	0.0058%
LCO	99.4%	0.005%	99.562%	0.000%	0.287%	0.145%	0.0072%

Metal(mol)= Ni+Co+Mn+Mg+Ti+Al (mol)

Table S3. Refined crystallographic data from the XRD patterns of pristine LCNO and LCO.

LCNO	Ion	Site	x	y	z	Occupancy
	Li^+	3a	0	0	0	0.991(6)
a=2.81454(6) Å	Li^+	3b	0	0	0.5	0.009(7)
c=14.0625(3) Å	Co^{3+}	3b	0	0	0.5	0.949(4)
R_{wp} = 10.03%	O^{2-}	6c	0	0	0.240181	1.0(4)
R_p = 6.68%	Ni^{3+}	3b	0	0	0.5	0.042(6)
S = 1.1158	$Ni^{2+\alpha}$	3a	0	0	0	0.008(6)
(003)/(104) = 1.78	$Co^{2+\beta}$	3a	0	0	0	0.001(6)
LCO	Ion	Site	x	y	z	Occupancy
	Li^+	3a	0	0	0	0.998(4)
a=2.81445(8) Å	Li^+	3b	0	0	0.5	0.002(5)
c=14.0568(4) Å	Co^{3+}	3b	0	0	0.5	0.998(5)
R_{wp}= 11.53%	O^{2-}	6c	0	0	0.239128	1.0(6)
R_p = 6.73%	$Co^{2+\beta}$	3a	0	0	0	0.002(6)
S = 1.2246						
(003)/(104) = 1.81						

Table S4. Energy density information for LCNO/Gr and LCO/Gr full-cells.

Electrode specification			
Electrode area (cm^2)	Cathode : 5.00		Anode : 5.94
Sample	LCNO	LCO	Spherical graphite (Gr)
Loading level (mg cm^{-2})	13.60	13.60	7.15
Electrode thickness (µm)	49.87	49.87	61.33
	Al foil thickness of 15µm included.		Cu foil thickness of 18µm included.
Separator thickness (µm)	10		
N/P ratio	1.10 ± 0.02		
Formation step testing condition	Voltage range: 3.0 – 4.35V Charge/discharge current density: 0.204 mA cm^{-2}		
Full-cell information			
Type	LCNO/Gr		LCO/Gr
Cell discharge capacity (mAh)	10.820		11.001
Average operating voltage (V)	3.82		3.83
Energy density estimation			
Type	LCNO/Gr		LCO/Gr
Initial volumetric energy density (Wh l^{-1})	682.0		695.2
Initial gravimetric energy density (Wh kg^{-1})	667.9		680.9

Table S5. Refined crystallographic data from the XRD patterns of 100th-cycled LCNO and LCO.

100th-cycled LCNO	Ion	Site	x	y	z	Occupancy
	Li^+	3a	0	0	0	0.954(6)
a=2.81503(5) Å	Li^+	3b	0	0	0.5	0.046(7)
c=14.0804(3) Å	Co^{3+}	3b	0	0	0.5	0.934(4)
R_{wp} = 11.33%	O^{2-}	6c	0	0	0.248837	1.0(4)
R_p = 6.68%	Ni^{3+}	3b	0	0	0.5	0.020(5)
S = 1.2153	$Ni^{2+\alpha}$	3a	0	0	0	0.030(6)
(003)/(104) = 1.66	$Co^{2+\beta}$	3a	0	0	0	0.016(6)
100th-cycled LCO	Ion	Site	x	y	z	Occupancy
	Li^+	3a	0	0	0	0.9070(5)
a=2.81705(7) Å	Li^+	3b	0	0	0.5	0.0930(6)
c=14.1102(9) Å	Co^{3+}	3b	0	0	0.5	0.9070(6)
R_{wp}= 17.52%	O^{2-}	6c	0	0	0.239128	1.0(6)
R_p = 8.34%	$Co^{2+\beta}$	3a	0	0	0	0.0930(6)
S = 1.7784						
(003)/(104) = 1.51						

Table S6. Major components of the cathode-electrolyte interphase (CEI) spontaneously and electrochemically generated on high-energy layered cathode oxide upon electrochemical operation. In this study, we especially focus on the chemical species; (1) the polycarbonate, (2) fluorinated organic species and (3) metal fluoride, which were commonly observed in the CEI.

Component	Chemical species of interest	Details
LiF, MF_x (Metal fluoride)	LiF_2^-, CoF^-, CoF_3^-	Commonly observed in electrolyte with commonly used fluorinated salt such as $LiPF_6$. Metal fluoride, including LiF, can be generated from reaction between semicarbonates (or cathode material) and HF. Furthermore, typical dissolution products of active materials in electrolyte, particularly with the presence of acidic species due to hydrolysis of PF_6^-.
RCF_x, RCO_xF_y	C_3OF^-, C_2F^- CH_2^-, *etc.*	Organo-fluorine compounds are usually formed when carbonate-based solvents in electrolyte solution react with HF.
Polycarbonate	CH_2^-, C_2HO^-, CH_3O^-	The possible route for formation of polycarbonates compound is generally accepted to be the oxidative polymerization of cyclic carbonates, e.g. ethylene carbonate, in electrolyte. [10, 11]
$ROCO_2Li$	CH_2^-, C_2HO^-, CH_3O^-	Semicarbonates are generally generated in carbonate containing electrolyte, such as ethylene, diethyl, or dimethyl carbonates.

Table S7. Concentration of dissolved Co and Ni in electrolyte of LCO/Gr and LCNO/Gr pouch-type full cell at 45°C after each specific cycle.

Sample	Electrolyte collected from LCO/Gr		Electrolyte collected from LCNO/Gr	
	Co (ppm)	Ni (ppm)	Co (ppm)	Ni (ppm)
100 cycles	80.76 ± 5.22	/	12.52 ± 3.11	0.01 ± 0.01
200 cycles	382.11 ± 13.11	/	92.11 ± 6.38	0.03 ± 0.01

Supplementary Note

Note S1. Estimation for volumetric- and gravimetric-energy density of full cell.

$$\text{Volumetric Energy density} \ (\text{Wh L}^{-1}) = \frac{(\text{Cell capacity}) \times (\text{Average voltage})}{(\text{Electrode area}) \times (\text{Total thickness of electrode including Al, Cu foil and separator})}$$

$$\text{Gravimetric Energy density} \ (\text{Wh kg}^{-1}) = \frac{(\text{Cell capacity}) \times (\text{Average voltage})}{(\text{Electrode area}) \times (\text{Loading level}) \times (\text{Electrode composition})}$$

Note S2. Plotting the relaxed potential curve from the collected GITT results.

At finite charge/discharge rate, the measured voltage differs from its thermodynamic voltage under open circuit condition (OCV) by an overpotential, which can be calculated from GITT measurements. We now read the thermodynamic voltage from the voltage after each relaxation/rest step, which is plotted in the y-axis of Figure 2e,f in the main text. The x-axis, charge/discharge capacity is the accumulative charge of all titration steps, which however differs for differently cycled electrode because the electrode cannot be fully charged/discharged in the previous/present cycle again due to overpotential. Therefore, to correct this systematic error and compare the charge/discharge curve under OCV of different cycled electrodes, we shifted the entire charge/discharge curve by a constant on the x-axis for the GITT data collected after 50th and 100th cycles. This constant was obtained by trial and error so that the charge/discharge curves of 1st, 50th and 100th cycled data best coincide with each other.

Note S3. High Loss EELS analysis.

For high loss analysis, the spectrums were calibrated by the highest intensity of the O-K main edge. O-K edge was background subtracted by a power law background. For Co L_3/L_2 ratio calculations, a step background with 2:1 ratio for L_3 vs. L_2 transitions was used to account for orbital degeneracy.[12] The ratio is then calculated by dividing the intensities for the two white lines.
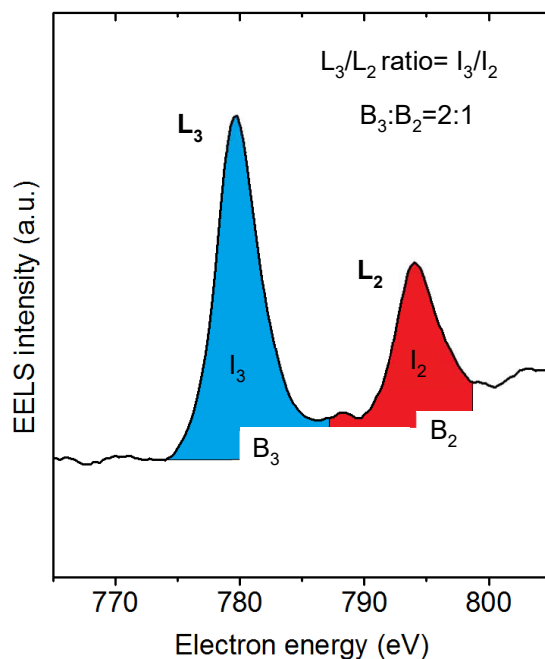
References

[1]   S. J. Kang, T. Mori, S. Narizuka, W. Wilcke, H.-C. Kim, *Nat. Commun.* **2014**, 5, 3937.

[2]   G. Kresse, J. Furthmüller, *Computational Materials Science* **1996**, 6, 15.

[3]   J. P. Perdew, K. Burke, M. Ernzerhof, *Physical Review Letters* **1996**, 77, 3865.

[4]   G. Kresse, D. Joubert, *Physical Review B* **1999**, 59, 1758.

[5]   S. L. Dudarev, G. A. Botton, S. Y. Savrasov, C. J. Humphreys, A. P. Sutton, *Physical Review B* **1998**, 57, 1505.

[6]   K. Momma, F. Izumi, *J. Appl. Crystallogr.* **2011**, 44, 1272.

[7]   W. Li, A. Dolocan, P. Oh, H. Celio, S. Park, J. Cho, A. Manthiram, *Nat. Commun.* **2017**, 8, 14589.

[8]   K. Edström, T. Gustafsson, J. O. Thomas, *Electrochim. Acta* **2004**, 50, 397.

[9]   P. Verma, P. Maire, P. Novák, *Electrochim. Acta* **2010**, 55, 6332.

[10]   M. Gauthier, T. J. Carney, A. Grimaud, L. Giordano, N. Pour, H.-H. Chang, D. P. Fenning, S. F. Lux, O. Paschos, C. Bauer, F. Maglia, S. Lupart, P. Lamp, Y. Shao-Horn, *J. Phys. Chem. Lett.* **2015**, 6, 4653.

[11]   I. A. Shkrob, Y. Zhu, T. W. Marin, D. Abraham, *J. Phys. Chem. C* **2013**, 117, 19255.

[12]   Z. L. Wang, J. S. Yin, Y. D. Jiang, *Micron* **2000**, 31, 571.